



# VCU

Virginia Commonwealth University  
VCU Scholars Compass

---

Theses and Dissertations

Graduate School

---

2016

## Electric Field Controlled Strain Induced Switching of Magnetization of Galfenol Nanomagnets in Magneto-electrically Coupled Multiferroic Stack

Hasnain Ahmad

Follow this and additional works at: <https://scholarscompass.vcu.edu/etd>

 Part of the [Electronic Devices and Semiconductor Manufacturing Commons](#), [Nanoscience and Nanotechnology Commons](#), and the [Nanotechnology Fabrication Commons](#)

© The Author

---

Downloaded from

<https://scholarscompass.vcu.edu/etd/4387>

This Dissertation is brought to you for free and open access by the Graduate School at VCU Scholars Compass. It has been accepted for inclusion in Theses and Dissertations by an authorized administrator of VCU Scholars Compass. For more information, please contact [libcompass@vcu.edu](mailto:libcompass@vcu.edu).

ELECTRIC FIELD CONTROLLED STRAIN INDUCED SWITCHING OF  
MAGNETIZATION OF GALFENOL NANOMAGNETS IN MAGNETO-ELECTRICALLY  
COUPLED MULTIFERROIC STACK

A Dissertation submitted in partial fulfillment of the requirements for the degree of Doctor of  
Philosophy in Engineering at Virginia Commonwealth University.

by

HASNAIN AHMAD

Bachelor of Science in Electrical and Electronic Engineering, Bangladesh University of  
Engineering and Technology, 2011

Doctoral committee chairperson: Prof. Supriyo Bandyopadhyay  
Commonwealth Professor, Department of Electrical and Computer Engineering

Virginia Commonwealth University  
Richmond, Virginia  
June, 2016

## **Acknowledgement**

I would like to begin acknowledgement by expressing sincere heartfelt gratitude to my PhD supervisor Prof. Supriyo Bandyopadhyay. His mentorship has been a tremendous force behind my development as a professional researcher. He guided me to become an experimentalist and brought out the potential in me through his teaching, profound understanding of my research and sometimes, a mere nudge in the right direction to see a complex problem in the simplest way and solve it in the most effective manner. I am also extremely thankful to him for giving me an opportunity to do research in National Institute of Standards and Technology (NIST), where I got in touch with many experimental researchers, scientists from whom I learnt a lot and experienced how I should lead life as a scientist. He gave me a chance to present my work in scientific conferences where I got exposed to advanced scientific communities. Without a doubt, his mentorship and wisdom will forever be the flagship in my life and enabling me to embark on a journey as an experimental scientist. I am also thankful to Dr. Jayasimha Atulasimha who has always graciously endowed me with his keen insight, advice and has been an instrumental figure in crafting my successful dissertation.

I have come to know and appreciate the guidance of some of the most intelligent people as my PhD committee member. I would like to show my earnest gratitude to Prof. Ümit Özgür and Dr. Avik Ghosh for their invaluable advice and meaningful critique. I thank Prof. Gary M. Atkinson who taught and trained me in micro fabrication tools and techniques and has always provided insightful advice. I thank Prof. Puru Jena for being a part of my PhD committee and helping me comprehend many complex theories of Physics and developing a clear perception of my research.

I am thankful to my friends and colleagues for their extraordinary support during this endeavor and I am extremely fortunate to share ideas with them, namely, Md. Iftekhar Hossain, Ayan Kumar Biswas, Md Mamun Al-Rashid, Dhritiman Bhattacharya, Pallabi Sutradhar, Md. Ahsanul Abdeed, and Justine Drobitch. Special thanks go to Dr. Noel D'Souza and Vimal Ganapathy Sampath who helped me develop expertise in sophisticated tools I have used in my research. I also offer my thanks to the staffs of the Electrical and Computer Engineering department, Joshua P Starliper of Wright Virginia Microelectronics Center, and my cordial gratitude to Dr. Dmitry Pestov and Dr. Carlos Castano Londono for their training, advice to use the facilities in Nanomaterials Characterization Center. Use of facilities at CNST, and NIST-Gaithersburg are gratefully acknowledged. Final professional acknowledgements go to the National Science Foundation (NSF) under the NEB2020 grant ECCS-1124714 SHF Grant CCF-1216614 and NSF CAREER grant CCF-1253370 as well as the Semiconductor Research Company (SRC) under NRI task 2203.001 for funding this research.

I cannot think of ending my acknowledgement without thanking my parents, Hosneara Monju, Shams Uddin Ahmad and my younger brother Hasib Ahmad, for their unending love, and prayer. They always helped me stride towards the path of success and empowered me with their guidance and support even at times when I was at my lowest. I will forever be grateful and indebted to their support.

# Table of Contents

<b>Acknowledgement</b> .....	<b>II</b>
<b>List of Figures</b> .....	<b>VI</b>
<b>List of Tables</b> .....	<b>IX</b>
<b>Chapter 1. Introduction</b> .....	<b>1</b>
1.1. Background of Straintronic Device and Villari Effect.....	1
1.2. Motivation of Using Galfenol as the Magnetostrictive Material .....	4
<b>Chapter 2. Fabrication of Galfenol Nanomagnets and Experimental Setup</b> .....	<b>7</b>
2.1: Galfenol Deposition and characterization .....	7
2.1.1: X-Ray Diffraction Analysis of Thin Film Galfenol .....	8
2.1.2 X-Ray Photoelectron Spectroscopy Analysis of Galfenol.....	13
2.1.3 M-H measurement of Galfenol Thin Film by Vibrating Sample Magnetometer: .....	14
2.2: Experimental Setup .....	16
2.2.1: Substrate Selection, Poling and Strain Measurement: .....	16
2.2.2: Shape and Stress Anisotropy Calculations of Nanomagnets:.....	18
2.2.3: Nano-Fabrication with Electron Beam Lithography .....	20
2.2.4: Material Deposition and Lift-off .....	21
2.2.5: Magnetic Force Microscopy Imaging of Nanomagnets: .....	23
<b>Chapter 3. Demonstration of Electric Field Control of Magnetization Switching in FeGa Nanomagnets</b> .....	<b>25</b>
3.1: Isolated Nanomagnets .....	25
3.2: Dipole Coupled Nanomagnets .....	30
3.3: Implementation of NOT Logic gate or Inverter: .....	33

<b>Chapter 4. Reversible Strain-induced Magnetization Switching in FeGa Nanomagnets- A Scheme to Realize Straintronic Memory Cell .....</b>	<b>34</b>
4.1: Background and Experimental Setup.....	34
4.2: MFM imaging of First Cycle of Compressive and Tensile Stress .....	36
4.3: MFM imaging of Second Cycle of Compressive and Tensile Stress.....	40
4.4: Implementation in a Straintronic Memory Scheme: .....	41
4.5 Energy Calculation .....	43
<b>Chapter 5. Repeatable ~180° Switching of Magnetization of Nanomagnets by Localized Strain.....</b>	<b>45</b>
5.1 Experimental Setup .....	46
5.2 ~180° Magnetization Switching .....	48
Case 1: Nanomagnets (198 x 183 x 10) nm <sup>3</sup> .....	48
Case 2: Nanomagnets (294 x 272 x 11) nm <sup>3</sup> .....	50
5.3 Repeatable 180 <sup>0</sup> Switching between 2 Stable Orientation .....	52
<b>Chapter 6. Conclusion .....</b>	<b>55</b>
<b>List of References.....</b>	<b>57</b>

## List of Figures

Figure 1.1: Schematic representation of 2 phase multiferroic system	2
Figure 1.2: Schematic representation of Spin reversal in a multiferroic MTJ	3
Figure 2.1.1: Magnetostriction vs Atomic Percentage, $x$ (%Ga)	7
Fig 2.1.2: Grazing incidence out of plane X-Ray diffraction pattern of 50 nm thin film Galfenol. The red curve is the experimental data and the blue curve is the fitted plot.	9
Figure 2.1.3: Grazing incidence out of plane X-Ray diffraction pattern of 15 nm thin film Galfenol. The red curve is the experimental data and the blue curve is the fitted plot	11
Figure 2.1.4: Grazing incidence in-plane X-Ray diffraction pattern from planes along the growth direction of 15 nm thin film Galfenol. The red curve is the experimental data and the blue curve is the fitted plot	12
Figure 2.1.5: X-Ray Photoelectron Spectroscopy analysis of 15 nm thick Galfenol film. The blue, red and green plots correspond to the distribution of atomic percentage of Fe, Ga and O respectively	13
Figure 2.1.6: Magnetization curves with the magnetic field in-plane and perpendicular-to-plane. The results are plotted for two different temperatures. (a) 300K, (b) 77K	15
Figure 2.1.7: Magnetization curve of a FeGa sputtered thin film at low magnetic fields at 77 K and 300K. The shape of the curve bears telltale sign of multiple phases with multiple coercivities as observed before in ref [22]	16
Figure 2.2.1: Strain response curves for bulk (001) PMN-PT substrate of dimensions 5x5x0.5 mm <sup>3</sup> . Poling of the substrate is performed in a castor oil bath with an electric field of 800 kV/m ( $V = 4$ kV). Measurement of the strain response of the poled substrate is then carried out for various fields. A linear strain response can be observed, with a strain of ~300 ppm generated for $V = 1.5$ kV and ~400 ppm for $V = 2$ kV [1]	17
Figure 2.2.2: Undercut developed for bilayer PPMA resist spun on PMN-PT substrate	21
Figure 2.2.3: Schematic picture of sputtering machine and normal deposition on the sample. Therefore, we deposit without rotation of the sample and additionally, care is taken to make the line of sight of the sputtering perpendicular to the sample surface to reduce side wall coverage even more.	22
Figure 2.2.4: Scanning electron microscopy image of nanomagnets.	24
Figure 3.1.1: (a) Magnetic force (MFM) and atomic force (AFM) micrographs of isolated elliptical nanomagnets that have been subjected to a strong magnetic field in the direction indicated by the vertical green arrow. The resulting magnetization direction of the right nanomagnet is indicated by the slanted red arrow. (b) The MFM image of the nanomagnets after they have been stressed with an electric field and relaxed (stress withdrawn). The magnetization direction of the left	26

nanomagnet does not show any discernible change, but the right nanomagnet's magnetization has rotated to a new orientation shown by the slanted solid yellow arrow. For comparison, the initial orientation of this nanomagnet's magnetization is shown by the broken red arrow. The magnetization has rotated by  $\sim 40^\circ$  owing to the stress generated by the electric field and subsequent removal of the electric field has not returned the magnetization to the original state, but left it in the new state. (c) The poling direction and direction of electric field applied to generate compressive stress along the nominal major axes of the nanomagnets.

Figure 3.1.2: (a) Same as figure 1(a), except there are four nanomagnets in this image. The initial magnetization direction of the nanomagnet in the upper right corner is indicated by the slanted red arrow. (b) MFM image after application and removal of stress. The magnetizations of all nanomagnets except the one in the upper right corner show no discernible difference between the pre- and post-stress conditions, but the magnetization of the one in the upper right corner has rotated by  $\sim 82^\circ$ . Notice that this nanomagnet is most 'circular' of all and therefore has the lowest shape anisotropy energy barrier, which is why stress was able to rotate its magnetization 29

Figure 3.2.1: Dipole-coupled pairs where the right partner is much more shape anisotropic than the left partner, making the right partner hard and the left partner soft. (a) MFM image after being magnetized by a magnetic field in the direction of the green vertical arrow and before application of stress. (b) MFM image after application and removal of stress. The magnetizations of all pairs, except the one in the upper right corner, show no discernible difference between the pre- and post-stress conditions, but the magnetization of the soft nanomagnet in the upper right corner (indicated by the short light green arrow) has rotated by  $\sim 110^\circ$ . 31

Figure 3.2.2: (a) MFM image of a dipole-coupled pair after being magnetized by a magnetic field in the direction of the green vertical arrow and before application of stress is shown on the left. In these pairs, the left partner is more shape-anisotropic than the right, i.e., the left nanomagnet is 'hard' and the right nanomagnet is 'soft'. MFM image after application and removal of stress is shown on the right. The magnetizations of all except the pair in the upper right corner show no discernible difference between the pre- and post-stress conditions, but the magnetization of the soft nanomagnet in the upper right corner (indicated by the short light green arrow) has rotated by  $\sim 150^\circ$ . (b) Similar to (a), except now the rotation is by  $180^\circ$ . 32

Figure 4.1: (a–c) Non-toggle straintronic memory of the type discussed in refs 10,11. (a) A magnetic field applied along the minor axis of an elliptical nanomagnet gives rise to two stable magnetization orientations at an angle with each other (the angle depends on the magnetic field strength, shape of the nanomagnet, etc.). They encode bits '0' and '1'. (b) We will assume that the magnetostriction coefficient of the nanomagnet is positive. Then, compressive stress along an axis collinear with one stable state (say, state 2) causes the magnetization to settle into state 1. If the magnetostriction coefficient were negative, the magnetization would have settled into state 2. (c) Tensile stress along the same axis causes the magnetization to settle into state 2 for positive magnetostriction and state 1 for negative magnetostriction. Therefore, we can write either bit by choosing the sign of the stress along the stress axis. We do not need to know what the previously stored bit was in order to write the desired bit. (d) Our test set-up. Electric field in the direction of substrate poling generates tensile stress in the nanomagnets whose major axes are aligned collinear with the poling direction. This aligns the magnetizations along one direction and writes bit '0'. Electric field in the opposite direction generates compressive stress and aligns the magnetizations in a different direction, writing bit '1'. 35

Figure 4.2.1: Magnetic force (MFM) and atomic force (AFM) micrographs of three isolated elliptical FeGa nanomagnets that have all been magnetized with a magnetic field in the direction 37

indicated by the thick vertical green arrow. Starting from the left, the first vertical panel shows the AFM image of the nanomagnet, the second vertical panel shows the initial magnetization state after magnetizing with the field (note that the magnetization is not always in the direction of the field), the third vertical panel shows the new magnetization state after compressive stress is applied and withdrawn, and the last vertical panel shows the magnetization state after tensile state is applied and withdrawn. Note that compressive stress takes the magnetization to a state different from the initial one and keeps it there after stress withdrawal (non-volatile). Tensile stress brings it back to the original state and keeps it there after stress withdrawal. Thus, tensile stress always writes the bit '0' and compressive stress writes a bit that is 'not-0' and we call it bit '1'. This realizes a non-volatile, non-toggle memory.

Figure 4.2.2: Same as figure 4.2.1, but for a different set of nanomagnets. Here, the nanomagnet in the last row was magnetized in a direction almost perpendicular to the magnetizing field showing that there is a deep energy minimum corresponding to that orientation and the nanomagnet prefers to go there even in the presence of the magnetizing field. Compressive stress, however, seems to drive it out of that state, but subsequent application of tensile stress brings it back to that state, just like in the case of the other nanomagnets. Again, a non-volatile, non-toggle memory is implemented. 38

Figure 4.3: Magnetic force microscope images of nanomagnets showing repeatability of the switching. A nanomagnet cycles through its two magnetization states repeatedly with successive compression and tension. Whenever the stress is tensile, the magnetization goes into one state and whenever stress is compressive, it goes into the other state. This consistency shows that the memory has endurance. 41

Figure 4.4: A straintronic memory array compatible with a crossbar architecture. Not drawn to scale. 42

Figure 5.1: Schematic of an elliptical shape nanomagnet and two pairs of square metal pad delineated on PMN-PT substrate (figure is not drawn to scale). The PMN-PT substrate has a dimension of  $(10 \times 10 \times 0.5) \text{ nm}^3$ . The major axis of the nanomagnet is aligned along the x direction. The substrate is poled along the thickness with the polarity shown in figure. Two pairs of Au pad are fabricated with the feature size of  $(400 \times 400 \times 0.08) \text{ nm}^3$ . In each pair, the pads are separated from each other by  $500 \text{ nm}$ , comparable to the thickness of the substrate. the line  $x_{AA'}$ , joining pads in pair AA' subtends an angle of  $30^\circ$  with x axis while line  $x_{BB'}$ , joining the pads in pair BB' subtends an angle of  $150^\circ$ . First, 300 volt is applied between the AA' pair and back electrode (shown in red), then while keeping the AA' activated, 300 volt is applied again between BB' pair and back electrode, next AA' is deactivated, finally BB' is deactivated. 47

Figure 5.2.2: Atomic force micrographs (AFM) and Magnetic force micrographs (MFM) of nanomagnets of dimensions,  $(294 \times 272 \times 11) \text{ nm}^3$ . Same as figure 3, a) shows the topography of the 4 nanomagnets. b) The magnets are initialized with a  $\sim 2$  Tesla magnetic field along the direction of the green arrow. c) The magnets were subjected to tensile stress. The magnetization of two nanomagnets in the top row (numbered as 1 and 2) have rotated  $180^\circ$  from their respective initial orientations (the initial states subtend a non-zero angle with applied field direction, as marked by white arrows in panel (b)). The nanomagnet, numbered as 3, has rotated less than  $180^\circ$ . It may happen due to pinning sites which might trap the magnetization. However, the newly acquired states of all three nanomagnets are single domain. 51

Figure 5.3: Atomic force micrographs (AFM) and Magnetic force micrographs (MFM) of two sets of nanomagnets (Set A and Set B) showing repeatable switching. Set A (a,b): 4 nanomagnets with 53

feature size (294 x 272 x 11) nm<sup>3</sup>, Set B (c,d): 4 nanomagnets with feature size (187 x 164 x 9) nm<sup>3</sup>. (a,c) Topography of the 4 isolated nanomagnets with negligible dipole interaction. (b,d) Left most panels show the MFM picture of the initial states; center panels show the MFM image after one tension cycle where nanomagnets (marked by white arrow in (b) and (d)) experienced 180° switching; right most panels show that the nanomagnets marked by white arrows have reverted to their initial orientation after second tension cycle.

## List of Tables

Table 1: Material properties of Co, Ni, Galfenol and Terfenol-D	4
Table 2.1: Deposition parameters for Galfenol Deposition	8
Table 2.1.1: Deposition parameters for Galfenol Deposition for 50 nm thin film	9
Table 2.1.2: List of 2-theta (degree), inter-planar distance (d), size of the grains and crystalline plane	9
Table 2.1.3: Deposition parameters for Galfenol Deposition for 15 nm thin film	10
Table 2.1.4: List of 2-theta (degree), inter-planar distance (d), size of the grains and crystalline plane	10
Table 2.1.5: List of 2-theta (degree), inter-planar distance (d), size of the grains and crystalline plane for the in-plane XRD analysis from the planes along the growth direction	11
Table 2.2.1: Material properties of PMN-PT and PZT	16
Table 2.2.2 Shape anisotropy, stress anisotropy values of different shapes of nanomagnets	19

## Abstract

The ability to control the bi-stable magnetization states of shape anisotropic single domain nanomagnets has garnered a lot of attention due to its potential for spawning non-volatile and energy-efficient computing and signal processing systems that can surpass conventional CMOS-based platforms. However, the magnetization switching methods in most popular approaches, namely using a magnetic field or spin transfer torque, consumes enormous amounts of energy which negates any advantage gained by a nanomagnet over a transistor. One way to circumvent this problem is to adopt a system of a 2-phase multiferroic nanomagnet, comprising a single domain magnetostrictive layer elastically coupled to a piezoelectric layer. A voltage applied on the piezoelectric layer generates a strain in it and the strain is elastically transferred to the magnetostrictive nanomagnet which rotates the magnetization states of the nanomagnet at room temperature via the converse magneto-electric effect. Such electric-field induced magnetization switching has been theoretically and experimentally shown to dissipate a minuscule amount of energy of only  $\sim 1$  attojoule at room temperature. Recently, it has been demonstrated that the magnetization of a single domain Co nanomagnet can be switched between two stable orientations by transferring a voltage-generated strain from a bulk PMN-PT substrate to the soft ferromagnetic Co layer. The switching probability, however, is low (4%). One of the reasons for low switching probability is the relatively small magnetostriction of elemental magnetostrictive nanomagnets like Co or Ni which would require relatively large electric fields to alter the magnetization state. One possible way to improve the statistics is to replace Co or Ni with a better magnetostrictive material like Galfenol. The alloy FeGa has much higher magnetostriction and is therefore desirable, but it also presents unique material challenges owing to the existence of many phases. Nonetheless, there is a need to step beyond elemental

ferromagnets and examine compound or alloyed ferromagnets with much higher magnetostriction to advance this field. There has been some work in FeGa thin films, but not in nanoscale FeGa magnets which are important for nanomagnetic logic and memory applications. This motivates my work.

We have designed and patterned FeGa nanomagnets of feature size ranging from 200 nm to 350 nm on a piezoelectric PMN-PT substrate and reported observation of a ‘non-volatile’ converse magneto-electric effect in elliptical FeGa. The nanomagnets are first magnetized with a magnetic field directed along their nominal major axes. Subsequent application of a strong electric field across the piezoelectric substrate generates strain in the substrate, which is partially transferred to the nanomagnets and rotates the magnetizations of some of them away from their initial orientations. The rotated magnetizations remain in their new orientations after the field is removed, resulting in ‘non-volatility’. In isolated nanomagnets, the magnetization rotates by  $< 90^\circ$  upon application of the electric field, but in a dipole-coupled pair consisting of one ‘hard’ and one ‘soft’ nanomagnet, which are both initially magnetized in the same direction by the magnetic field, the soft nanomagnet’s magnetization rotates by  $> 90^\circ$  upon application of the electric field because of the dipole influence of the hard nanomagnet. This effect can be utilized for a nanomagnetic NOT logic gate.

We have successfully demonstrated a reversible strain-induced magnetization switching between two stable/metastable states in  $\sim 300$  nm sized FeGa nanomagnets delineated on a piezoelectric PMN-PT substrate. Voltage of one polarity applied across the substrate generates compressive strain in a nanomagnet and switches its magnetization to one state, while voltage of the opposite polarity generates tensile strain and switches the magnetization back to the original state. The two states can encode the two binary bits, and, using the right voltage polarity, one can

write either bit deterministically. This portends an ultra-energy-efficient non-volatile “non-toggle” memory.

Finally, in order to enhance the repeatable switching probability, a scheme of using localized strain to alter the magnetization states of nanomagnets has been proposed and experimentally realized by fabricating two pairs of patterned gold metals pad on PMN-PT substrate. The nanomagnets are then grown and aligned in such a way that one pair of electrodes subtends an angle  $30^\circ$  with the common major axis of the magnets and the other pair subtends an angle  $150^\circ$ . The voltage was first applied between one pair of electrode and the ground plate on the back of the substrate and the other pair was activated. This method of applying voltage can completely reverse the magnetization of a nanomagnet with high probability. With correct voltage polarity, we have been able to switch the magnetization states of nanomagnets (feature sizes, 184-294 nm) between two stable orientations which are  $180^\circ$  apart in repeated cycle. This will enable writing of binary bits in non-volatile magnetic memory implemented with magnetotunneling junctions whose soft layers are two-phase magnetostrictive/piezoelectric multiferroics. This thesis establishes Galfenol as the potential candidate in strain induced non-volatile memory application. This will stimulate research in binary or ternary magnetostrictive alloys to exploit their unique properties to realize more efficient devices that can outperform their charge based counterparts. The work has also realized a method of generating high localized strain which can be utilized for repeatable switching with dissipation as small as 6143 kT which is at least two orders of magnitude less than what spin-transfer-torque memory STT-RAM dissipates in a write cycle.

# Chapter 1. Introduction

## 1.1. Background of Straintronic Device and Villari Effect

Exploiting electron's spin to encode binary information has shown promise for extremely energy efficient and nonvolatile logic and memory devices, [2]. In the traditional CMOS based devices, the on and off states are controlled by the number of charges  $N$  moving in and out of the active region which result in consumption of exorbitant amount of energy. A state-of-the-art CMOS dissipates over 50000 kT of energy at room temperature in isolation and over  $10^6$  kT in a circuit to switch at a few GHz of clock frequency [3]. On the other hand, if the binary bit information ('0' or '1') is stored in the spins of a nanomagnet, the switching between two stable/metastable states is ideally governed by the collective evolution of spins due to their mutual exchange interaction. Hence, the number of information carrier is ideally 1 and not  $N$ , which drastically reduces the energy dissipation. However, much of the advantage gained by the reduction of the number of information carriers is squandered in the writing scheme of a bit which involves switching the magnetization to the desired state by an external agent.

There are many schemes for altering the magnetization state of a nanomagnet to enable the writing of a bit. The oldest is to use a local magnetic field generated by an on-chip current, which is, regrettably, extremely dissipative [4] and would dissipate about  $10^7$  kT of energy at room temperature per write operation [3]. The second is to use a spin-polarized current to deliver a spin-transfer torque [5] or induce domain wall motion [6]. These are also extremely dissipative strategies and dissipate between  $10^4$  kT and  $10^7$  kT of energy per write step [7], [8]. The recent use of the giant spin Hall effect to generate a spin polarized current [9] may end up reducing the energy dissipation to perhaps  $\sim 10^4$  kT per step, but a much more energy-efficient approach is to

use two-phase multiferroics (a magnetostrictive nanomagnet delineated on a piezoelectric film) as shown in figure 1 [10]. An electrostatic potential applied across the piezoelectric film generates strain in that layer, which is partially transferred to the magnetostrictive layer and rotates the latter's magnetization via the **Villari effect**. This effect is based on the fact that when a mechanical stress is imposed on a sample, it alters the magnet's potential energy profile. That can rotate the magnet's magnetization while dissipating only  $\sim 100$  kT of energy to switch at a clock frequency of  $\sim 1$  GHz [10].

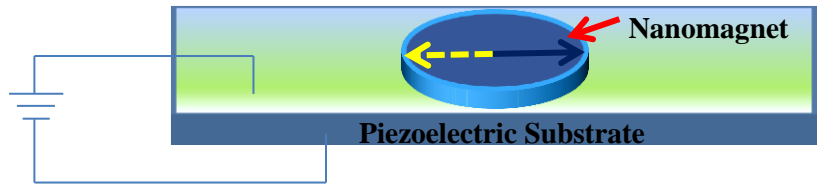


Figure 1.1: Schematic representation of 2 phase multiferroic system

The above effect can be exploited to implement a voltage-controlled resistance switch. For this purpose, one would fabricate a magneto-tunneling junction (MTJ) stack consisting of three layers – a hard magnetic layer whose magnetization is stiff and does not budge easily, a spacer layer through which electrons tunnel, and finally a soft magnetic layer whose magnetization can be easily rotated by voltage-induced stress. The resistance of the MTJ depends on the angle  $\theta$  between the magnetizations of the hard and soft layer. If the magnetizations are parallel ( $\theta = 0^\circ$ ), then the resistance is small, whereas if the magnetizations are anti-parallel ( $\theta = 180^\circ$ ), then the resistance is large. Therefore, by changing the magnetization of the soft layer, and hence by changing  $\theta$ , we can change the resistance of the MTJ. In general, the resistance of the MTJ is inversely proportional to  $1 + \eta_1 \eta_2 \cos \theta$ , where  $\eta_1$  and  $\eta_2$  are the spin filtering efficiencies

at the interfaces of the spacer layer with the hard and soft magnetic layers, respectively [11].

Therefore, the resistance ratio (MR) for  $\theta = 180^\circ$  and  $\theta = 0^\circ$  is

$$MR = \frac{1 + \eta_1 \eta_2}{1 - \eta_1 \eta_2} \quad (1.1)$$

Typical values of  $\eta$  are about 70% [12]; hence, the resistance ratio is roughly 2:1.

The switching of the soft layer of an MTJ upon application of stress is depicted in Fig. 1.

First, a strong magnetic field can be used to align the magnetizations of the soft and hard layer

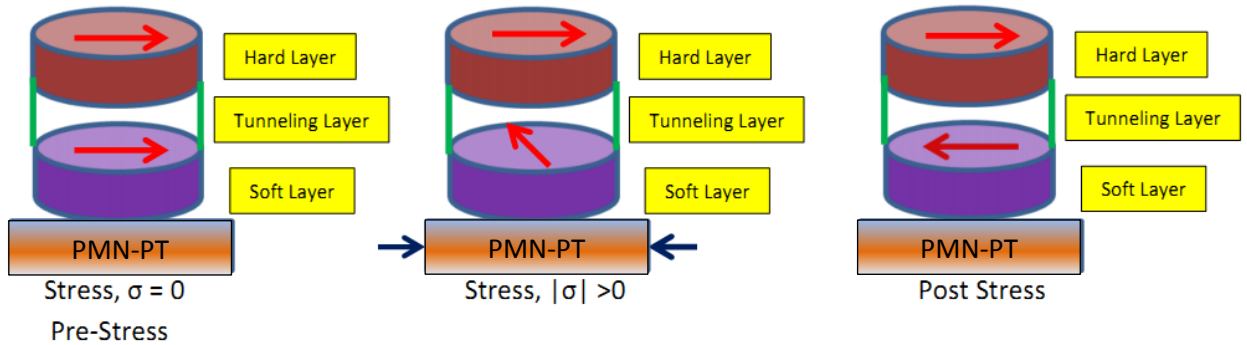


Figure 1.2: Schematic representation of Spin reversal in a multiferroic MTJ

along the field, so that they are mutually parallel. The MTJ resistance will be in the low state and encode, say, the logic bit 0. Next, a voltage is applied across the underlying piezoelectric substrate PMN-PT, which generates stress in the piezoelectric, which is transferred to the soft layer in elastic contact with the piezoelectric and rotates its magnetization by  $\sim 90^\circ$ . If we withdraw the stress immediately when the magnetization completes the  $90^\circ$  rotation, then residual torque acting on the magnetization vector will continue to rotate it and complete  $180^\circ$  rotation [13]. At that point, the hard and soft layers will have anti-parallel magnetizations and the MTJ resistance will be high, encoding, say, the logic bit 1.

## 1.2. Motivation of Using Galfenol as the Magnetostrictive Material

Our teams have shown for the first time, experimental demonstration of strain-clocked nanomagnetic logic utilizing single-domain Co nanomagnets of ~200 nm lateral dimensions on a bulk PMN–PT substrate to realize a Boolean NOT logic gate and unidirectional propagation of logic bit information down a chain of nanomagnets [1]. Although the nanomagnet dimensions are chosen so that stress anisotropy can beat the shape anisotropy barrier, issues such as lithographic variations and other discrepancies such defects, and jagged edges, which result in shape anisotropy energies that are higher than desirable or create pinning sites, may cause the effective field due to stress anisotropy energy to be insufficient to induce magnetization rotation. To improve the situation and generate large stress anisotropy in the nanomagnet, we have to investigate the unique magnetostrictive properties of binary or ternary alloy like Galfenol ( $\text{Fe}_x\text{Ga}_{1-x}$ ), Terfenol-D ( $\text{Tb}_x\text{Dy}_{1-x}\text{Fe}_2$  ( $x\sim 0.3$ )). Table 1 shows a comparative analysis of the material properties of different ferromagnetic materials.

Table 1: Material properties of Co, Ni, Galfenol and Terfenol-D

Material	Young's Modulus, $Y$ (GPa)	Saturation Magnetization, $M_s$ (A/m)	Magnetostriction Constant ( $3/2 \lambda_s$ )
Ni	214	$4.84 \times 10^5$	$-3 \times 10^{-5}$
Co	209	$14.22 \times 10^5$	$-5 \times 10^{-5}$
Galfenol ( $\text{Fe}_{80}\text{Ga}_{20}$ )	75	$11.9 \times 10^5$	$30-35 \times 10^{-5}$
Terfenol-D	25-35	$8 \times 10^5$	$90 \times 10^{-5}$

The stress anisotropy energy in a magnetostrictive material is governed by the following equation;

$$E_{StressAnisotropy} = \frac{3}{2} \lambda_s \sigma M_s V \quad (1.2)$$

where,  $\lambda_s$ ,  $\sigma$ ,  $M_s$ ,  $V$  are the magnetostriction coefficient, applied stress, saturation magnetization and volume respectively of the material. Hence, the stress needed to switch a magnetostrictive nanomagnet is inversely proportional to the magnetostrictive coefficient (the more magnetostrictive a material is, the easier it is to rotate its magnetization with stress). From table 1, we can see that Terfenol-D offers the highest magnetostriction value while Galfenol has less magnetostriction than Terfenol-D but offers much larger value than those of the elemental Co or Ni. But to grow a ternary alloy like Terfenol-D while maintaining correct stoichiometry is quite challenging. Galfenol, on the other hand, is expected to grow as polycrystalline material during sputtering using just one single target. Therefore, it may preserve some of its high magnetostriction properties of bulk single crystal. Moreover, Galfenol has higher saturation magnetization than Ni and Terfenol-D. This makes it all the more suitable for characterization with Magnetic Force Microscopy (MFM) because of higher contrast MFM images with minimal tip-induced magnetization reorientation. Nonetheless, to further advance the field of 2 phase multiferroic system, it is necessary to look at exquisite properties of binary or ternary alloys. Galfenol provides the most balanced characteristics among the novel materials. There has been some work in FeGa thin films [14]–[17], but not in nanoscale FeGa magnets which are important for nanomagnetic logic and memory applications. This motivates our quest.

The rest of the work is divided into four chapters. The second chapter discusses the material growth and characterization of Galfenol, shape and stress anisotropy calculations, experimental setup for electron beam nanolithography and magnetic force microscopy. The third

chapter describes the magnetization switching of isolated and dipole coupled pair of Galfenol nanomagnets. It illustrates the metastable behavior of the magnetization states of Galfenol and how it can be utilized in nanomagnetic logic operation. The fourth chapter discusses the first experimental demonstration of a stress induced reversible non-volatile non-toggle memory scheme using elliptical nanomagnets with feature size,  $\sim 300$  nm (major axis) by 240 nm (minor axis) which has the potential of dissipating minuscule energy while writing bit 1 with one polarity of stress and bit 0 with opposite polarity of stress deterministically. Finally, in the fifth chapter, we report experimental demonstration of repeatable switching between two stable orientations of the magnetization, which are  $180^\circ$  apart. The scheme also rules out any use of external feedback circuitry or magnetic field ensuing minimal energy consumption.

## Chapter 2. Fabrication of Galfenol Nanomagnets and Experimental Setup

### 2.1: Galfenol Deposition and characterization

As mentioned earlier in the introduction of the dissertation, the higher magnetostrictive a material is, the easier it is to rotate its magnetization with stress. Galfenol or  $\text{Fe}_{1-x}\text{Ga}_x$ , where  $x = 18$  atomic percentage, possesses high magnetostriction. The following is a typical saturation magnetostriction value  $\lambda_s$  vs atomic composition  $x$  (Galium) plot [18], [19]:

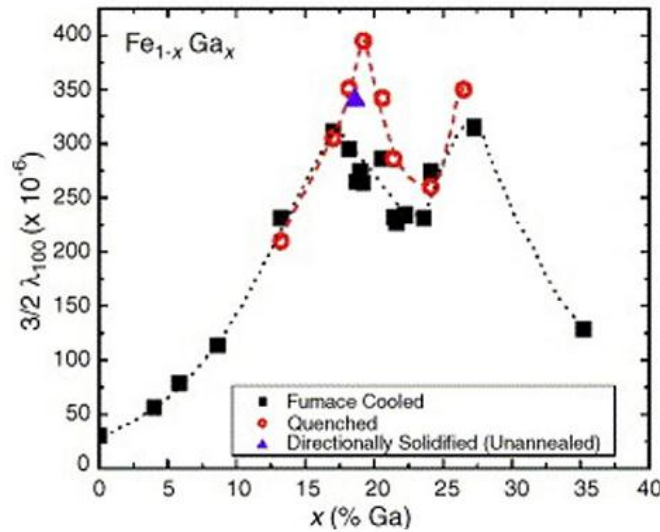


Fig 2.1.1: Magnetostriction vs Atomic Percentage,  $x$  (%Ga) [17]

In a single crystalline  $\text{Fe}_{1-x}\text{Ga}_x$  where Ga atomic percentage varies from 17% to 20%, the value of  $\lambda_s$  varies from 300 ppm to 400 ppm. Such a high value, if realized in practice, can be utilized for easy switching of the magnetization in the free layer as we apply voltage to the piezoelectric layer. Most studies show that FeGa contains a mixture of A2 (Disordered BCC Fe) and DO3 phase ( $\text{Fe}_3\text{Ga}$ ) [18]. To deposit FeGa, I have used sputtering machine at the Virginia

Microelectronics Center, VCU and the National Institute of Standards and Technology, Gaithersburg, Maryland. A typical deposition parameters for nanomagnets are given below:

Table 2.1: Deposition parameters for Galfenol Deposition

Power (Watt)	Deposition Pressure (milli-Torr)	Temperature (°C)	Time (sec.)	Base (Starting) pressure (Torr)
45	1	21	33-90	(1-3) $\times 10^{-8}$

### 2.1.1: X-Ray Diffraction Analysis of Thin Film Galfenol

To characterize the thin film for its crystallinity behavior, I carried out several grazing incidence XRD measurements at different power, time and pressure. These XRD patterns are taken carefully only from the thin film FeGa deposited on top of Silicon substrate so the peaks only correspond to the top layer and not from the substrate. We have carried out two types of grazing incidence X-Ray diffraction analysis depending on how the XRD detector collects the data. When the detector moves in the plane perpendicular to the thin film plane, it collects the data from the planes parallel to the crystal plane which we call out of plane grazing incidence XRD analysis. On the other hand, if the detector moves in the plane parallel to the crystal plane, it collects data from the planes along the film growth direction which we call in-plane grazing incidence XRD analysis.

Table 2.1.1 lists deposition parameters and Figure 2.1.2 shows the corresponding XRD pattern.

Table 2.1.1: Deposition parameters for Galfenol Deposition for 50 nm thin film

Power (Watt)	Deposition Pressure(milli-Torr)	Temperature (°C)	Time (sec.)	Base (Starting) pressure (Torr)
100	6.6	21	33-90	$(1-3) \times 10^{-6}$

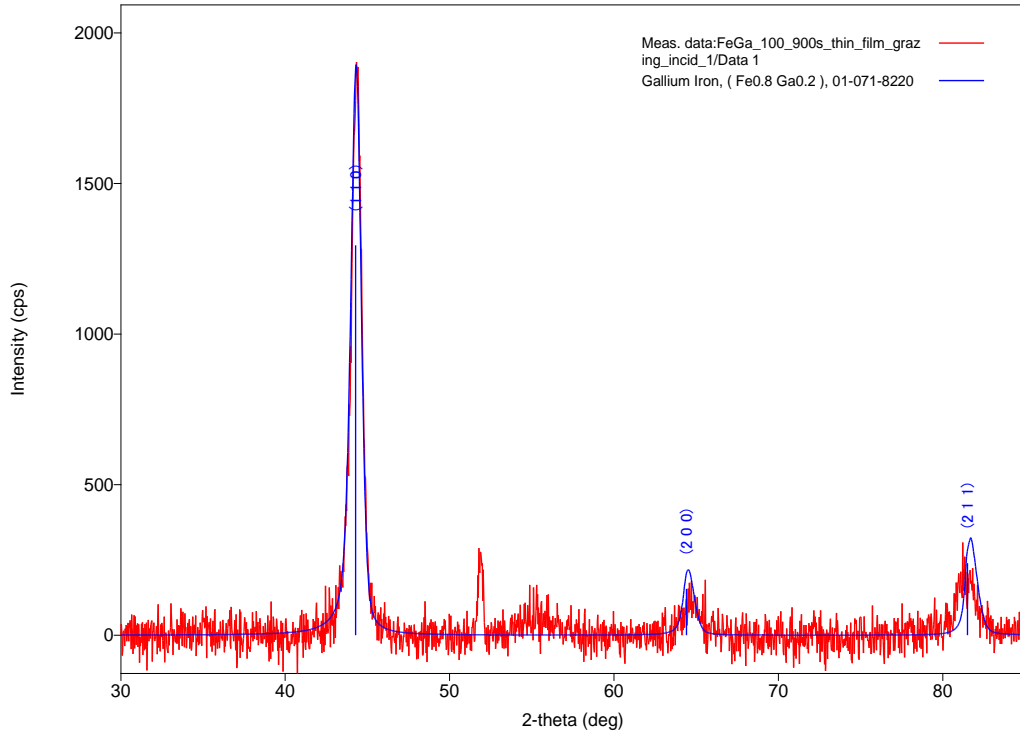


Fig 2.1.2: Grazing incidence out of plane X-Ray diffraction pattern of 50 nm thin film Galfenol. The red curve is the experimental data and the blue curve is the fitted plot.

Table 2.1.2: List of 2-theta (degree), inter-planar distance (d), size of the grains and crystalline plane

2-theta (Degree.)	d(A°)	Size(A°)	Plane
44.320	2.0422	124.4	(110)
64.63	1.441	79	(200)
81.05	1.1855	82	(211)

To fabricate our final device, we need to deposit around 10 to 15 nm thin film Galfenol. Therefore, we have also carried out XRD for extremely thin (15nm to 19nm) sample and observed polycrystalline behavior. The following XRD pattern in figure 2.1.3 shows the intensities matching (110), (200), (211) planes and the ratios of intensities also matches with the powdered sample spectrum. It confirms qualitatively that our sample is randomly oriented polycrystalline with all possible orientations appearing. Table 2.1.3 and 2.1.4 lists information of deposition parameters and XRD studies respectively.

Table 2.1.3: Deposition parameters for Galfenol Deposition for 15 nm thin film

Power (Watt)	Deposition Pressure(milli-Torr)	Temperature (°C)	Time (sec.)	Base (Starting) pressure (Torr)
45	1	21	45	(1-3)x10 <sup>-8</sup>

Table 2.1.4: List of 2-theta (degree), inter-planar distance (d), size of the grains and crystalline plane

2-theta(Degree)	d (Å)	Size (Å)
44.178	2.0484	75.0
64.33	1.4470	41
81.65	1.1782	44

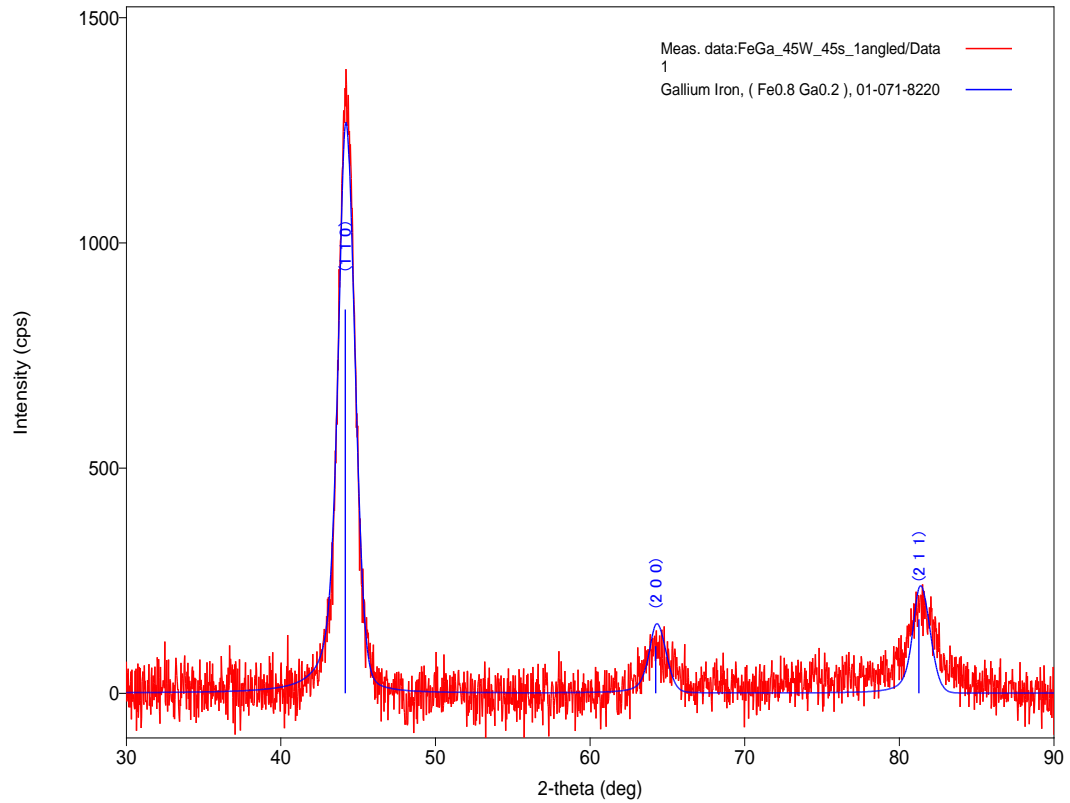


Fig 2.1.3: Grazing incidence out of plane X-Ray diffraction pattern of 15 nm thin film Galfenol. The red curve is the experimental data and the blue curve is the fitted plot.

We have performed in-plane XRD analysis (figure 2.1.4) on the 15 nm thick sample and interestingly found that there is a prominent (110) texture from the planes perpendicular to the sample plane or along the growth direction. At the same time, (200) and (211) orientations are all suppressed. Table 2.1.5 lists information of XRD studies.

Table 2.1.5: List of 2-theta (degree), inter-planar distance (d), size of the grains and crystalline plane for the in-plane XRD analysis from the planes along the growth direction

2-theta (Degree)	Size (Å <sup>0</sup> )
43.774	182.9

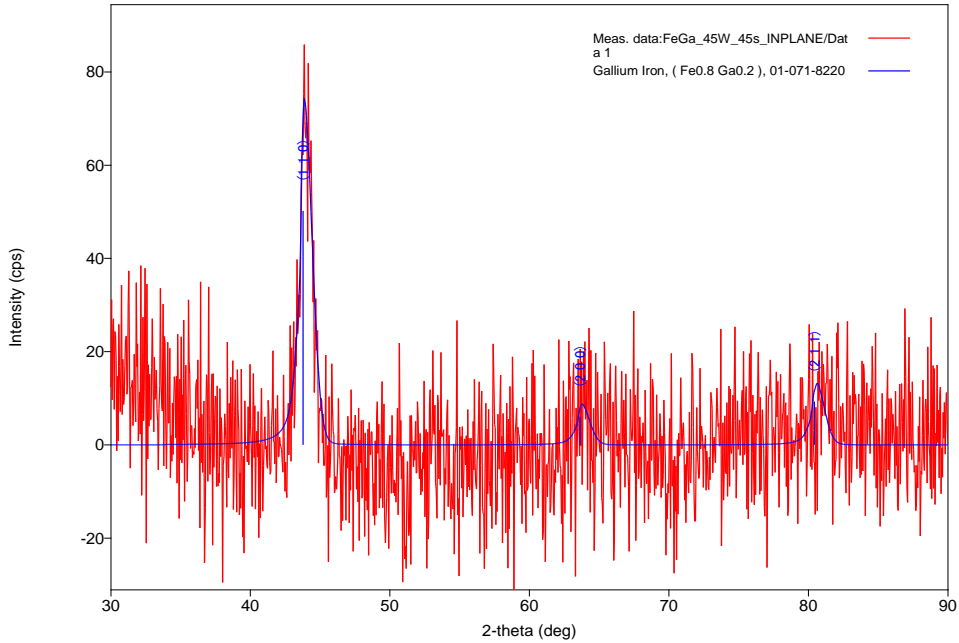


Fig 2.1.4: Grazing incidence in-plane X-Ray diffraction pattern from planes along the growth direction of 15 nm thin film Galfenol. The red curve is the experimental data and the blue curve is the fitted plot.

If we compare the grain sizes, the in-plane XRD gives larger grain size (182.9 Angstrom) compared to 75, 41 and 44 Angstrom in the out of plane XRD. This confirms the columnar structure of FeGa as mentioned in reference [20], [21]. In this case the length of the columnar grain closely matches the total thickness of the sample (16 nm). We conclude that with a sputtering power of 45 watt and very low pressure of 1 milli-torr, Galfenol growth is polycrystalline at best and has a continuous columnar feature along the growth axis.

## 2.1.2 X-Ray Photoelectron Spectroscopy Analysis of Galfenol

To perform compositional analysis, I carried out XPS (X-ray Photoelectron Spectroscopy). Depth profile has been obtained by XPS where the Ar ion etching has been done at 3kV, 1  $\mu$ A to 2  $\mu$ A to remove layers of thin film and then taking XPS data to get spectrum for the underlying layer until the spectrum of substrate silicon is found. The etching rate is 0.029 A<sup>o</sup>/s. Shown in Figure 2.1.5 is the layer by layer atomic ratio of Fe, Ga and O.

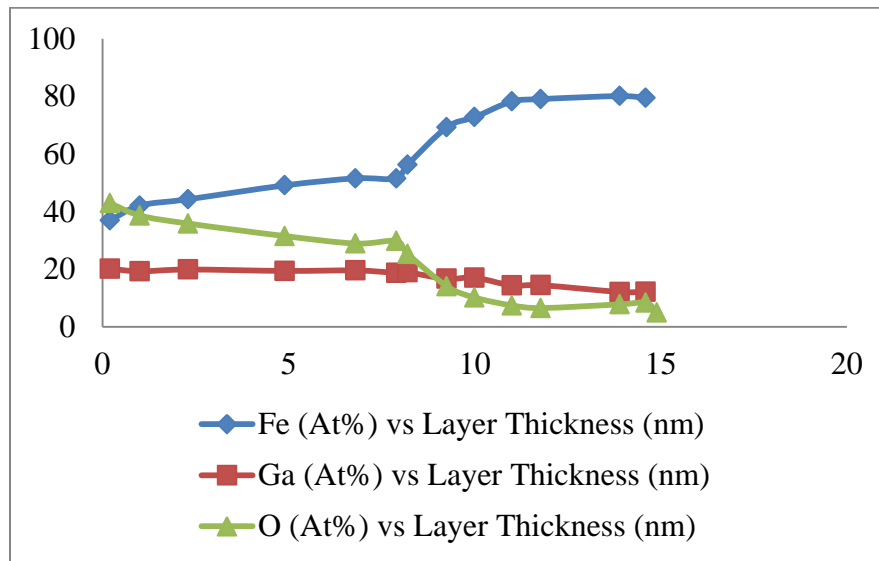


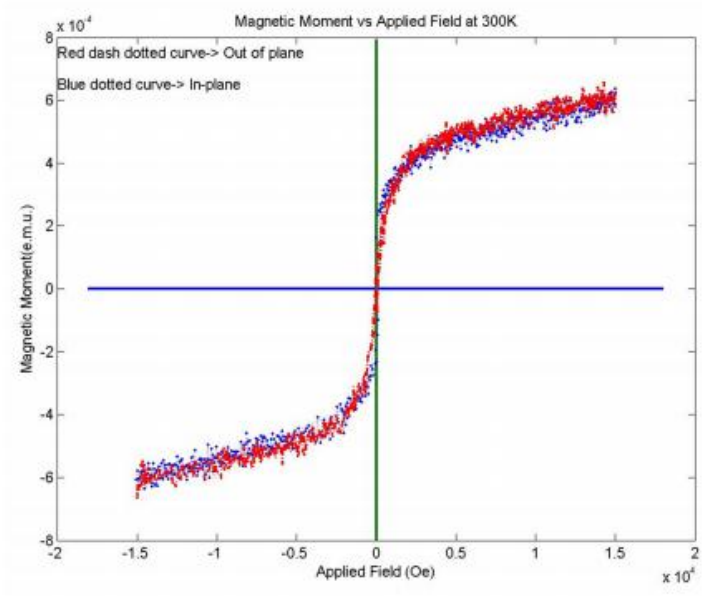
Fig 2.1.5: X-Ray Photoelectron Spectroscopy analysis of 15 nm thick Galfenol film. The blue, red and green plots correspond to the distribution of atomic percentage of Fe, Ga and O respectively.

As we can see, oxygen is diffused through half of the sample. It is due to the fact that we have not deposited any capping layer to cover the thin film. Another interesting fact is that Fe/Ga ratio increases as we go from the top layer to the bottom layer and near the silicon, the film mostly consists of Fe and Silicon alloy (iron silicide). That means Gallium tends to be located more near the surface. This means that in our thin film, there is a whole range of the value of  $\lambda_s$

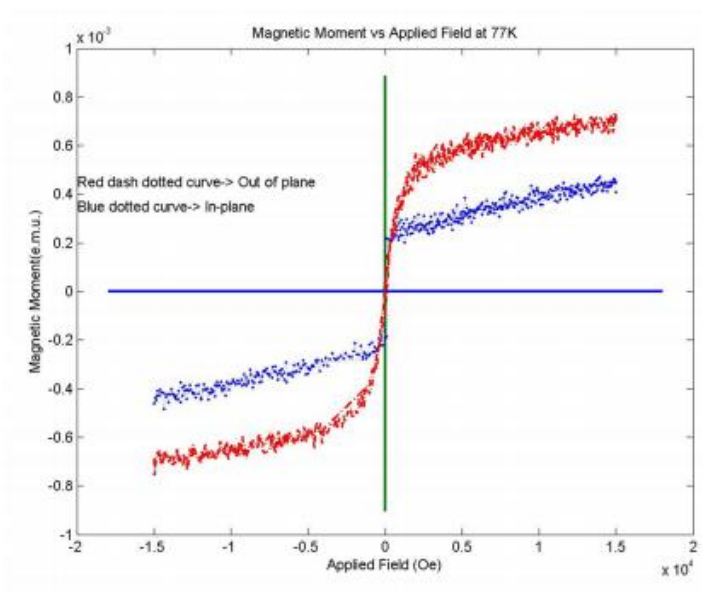
from 35% Gallium to 10% Gallium in the structure (see figure 2.1.1 again). The XRD and XPS analysis substantiate the fact that material properties of sputtered thin film of Galfenol deviates significantly from the (100) single crystalline bulk substrate. We took this into consideration when the shape anisotropy of different shapes and sizes of nanomagnets were calculated. The next section will elaborate on different material properties and theoretical calculations.

### 2.1.3 M-H measurement of Galfenol Thin Film by Vibrating Sample Magnetometer:

The magnetization (M-H) curves of FeGa layers were measured at 77 K and 300 K in a vibrating sample magnetometer and showed not only ferromagnetic behavior, but that the layer had in-plane magnetic anisotropy (see figure 2.1.6). The measured in-plane coercivity was ~180 Oe and the out-of-plane coercivity was ~120 Oe as shown in zoomed in figure 2.1.7. Interestingly, the M-H curves showed “shoulders” indicative of the presence of more than one phase in FeGa, each with a different coercivity, as previously noted in other materials [22]. This indicated the presence of multiple energy barriers in the potential profiles of the FeGa nanomagnets which could result in the formation of metastable magnetization states. Stress could always drive a nanomagnet into such a state where it will remain after stress is withdrawn since the state is “metastable” and robust against thermal perturbations at room temperature. Metastable magnetization states could, of course, arise from other effects as well, such as due to pinning sites or irregular geometry of the nanomagnets caused by imperfect electron-beam lithography. There is a recent report of non-Joulian magnetostriction in FeGa [23] which could further complicate the nanoscale switching.



(a)



(b)

Figure 2.1.6: Magnetization curves with the magnetic field in-plane and perpendicular-to-plane. The results are plotted for two different temperatures. (a) 300K, (b) 77K

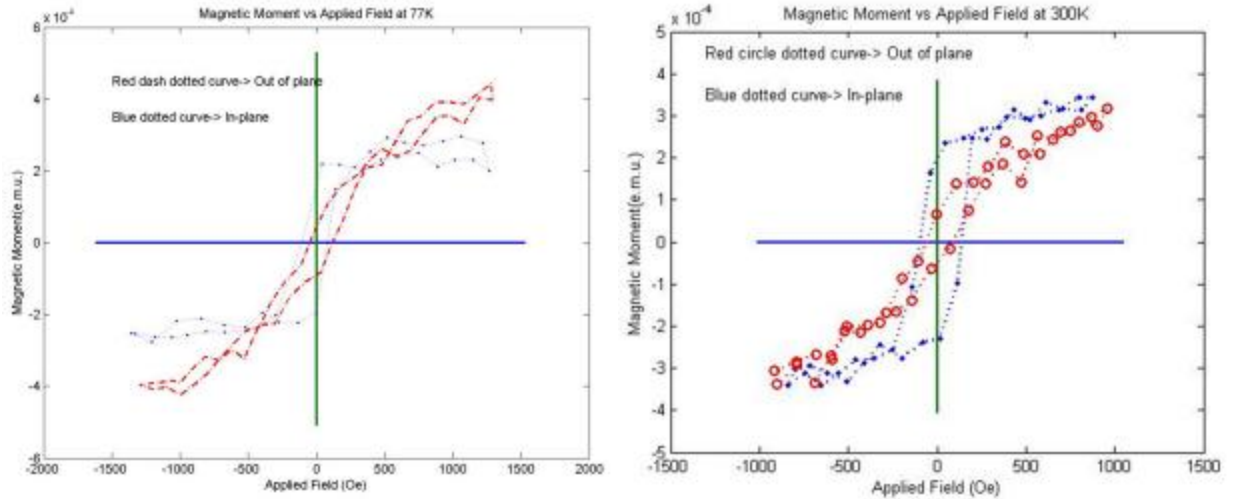


Figure 2.1.7: Magnetization curve of a FeGa sputtered thin film at low magnetic fields at 77 K and 300K. The shape of the curve bears telltale sign of multiple phases with multiple coercivities as observed before in ref. [22]

## 2.2: Experimental Setup

### 2.2.1: Substrate Selection, Poling and Strain Measurement:

The piezoelectric substrate used in our experiments was a polished (001)-oriented and (011) oriented PMN-PT substrate of dimensions  $5 \times 5 \times 0.5 \text{ mm}^3$  and  $10 \times 10 \times 0.5 \text{ mm}^3$  supplied by TRS technology and MTI Corporation. Table 2.2.1 shows material properties of PMN-PT and PZT.

Table 2.2.1: Material properties of PMN-PT and PZT

Property	Ceramic PZT-5H	PMN-PT Single Crystal X2B
$T_c$ ( $^{\circ}\text{C}$ )	>210	>142
$E_c$ (kV/cm)	7.8	1.9-2.5
$d_{33}$ (pm/V)	650-690	1500-2300
$d_{31}$ (pm/V)	-100	-1750
$k_{33}$	0.75	0.91-0.95

$k_t$	0.55	0.55-0.59
-------	------	-----------

Table 2.2.1 shows us that PMN-PT substrate offers significantly larger  $d_{33}$  and  $d_{31}$  coupling coefficients than those of PZT-5H substrates. We have used (001) oriented PMN-PT substrates to apply voltage across the length of the PMN-PT substrate (5mm x 5mm x 0.5 mm) to generate high strain owing to its high  $d_{33}$  coupling coefficient while the (011) oriented PMN-PT substrate has been used to apply voltage along the thickness (0.5 mm) to utilize its high  $d_{31}$  coupling coefficient. The stress and strain measurement of the PMN-PT sample has been carried out by our team member, Dr. Noel D'Souza. AT first, poling of the substrate is performed in a castor oil bath with an electric field of 800 kV/m ( $V= 4$  kV). A strain gauge is then attached to the PMN-PT substrate to measure in-plane strain. Measurement of the strain response of the poled substrate is then carried out for various fields. Figure 2.2.1 is showing the strain response when PMN-PT is subjected to electric field along the length [1].

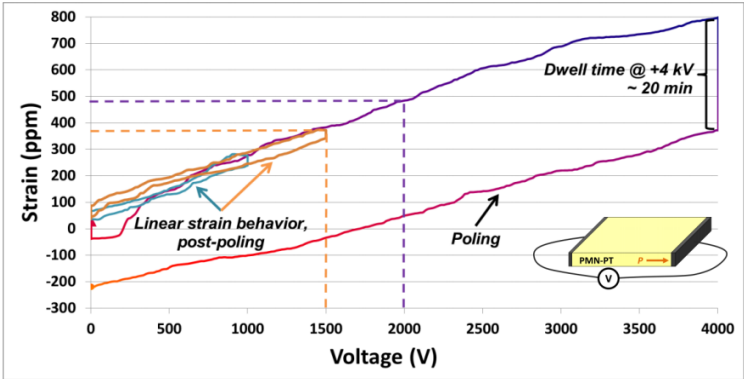


Figure 2.2.1: Strain response curves for bulk (001) PMN-PT substrate of dimensions 5x5x0.5 mm<sup>3</sup>. Poling of the substrate is performed in a castor oil bath with an electric field of 800 kV/m ( $V= 4$  kV). Measurement of the strain response of the poled substrate is then carried out for various fields. A linear strain response can be observed, with a strain of ~300 ppm generated for  $V = 1.5$  kV and ~400 ppm for  $V = 2$  kV [1].

It can be seen that in a linear regime, for a voltage of 1.5 kV ( $E = 300$  kV/m), a strain of  $\sim 300$  ppm is observed, while at  $V = 2$  kV ( $E = 400$  kV/m), a strain of  $\sim 400$  ppm can be generated. The  $d_{33}$  value of (001) PMN-PT experimentally measured in our experiments ( $\sim 1000$  pm/V) is in accordance with other experimentally derived  $d_{33}$  values from references [24], [25]. For our numerical calculations, we use the following material constants for a) FeGa: Young's modulus,  $Y = 75$  GPa (Davis, 2000), saturation magnetization,  $M_s = 11 \times 10^5$  A/m, (b) PMN-PT: Young's modulus,  $Y = 105$  GPa, Curie temperature,  $T_c = 150$  °C [21].

### 2.2.2: Shape and Stress Anisotropy Calculations of Nanomagnets:

It is extremely important to find a “sweet spot” where the shape anisotropy is sufficiently high to allow good magnetic force microscopy (MFM) imaging (with low moment MFM tips) but is low enough that the stress anisotropy energy due to applied stress overcome the shape anisotropy energy barrier in the magnet which is determined by the shape of the magnet, among other things.

To calculate the shape anisotropy energy, we need to know the saturation magnetization of the nanomagnet. The saturation magnetization is assumed based on an average over all the layers of 11nm to 12 nm film (ranging from 1200 emu/cc to 800 emu/cc) since different segments have different Fe/Ga atomic ratio. We opted for 960 emu/cc ( $9.6 \times 10^5$  A/m) since a large section from the top layer has higher Ga content. Since the composition of Ga varies with in the material, we also adopted an effective magnetostriction coefficient ( $\lambda_{\text{eff}}$ ) rather than the isotropic bulk value of  $\lambda_s$  (for single crystalline,  $3/2 * \lambda_s = 300$  to 400 ppm). From the XRD analysis, we found out that out of plane XRD has all possible orientations but in-plane XRD has strong (110) textures. The in-plane  $\lambda_{\text{eff}}$  can be calculated as  $2/5 \lambda_{100} = 73.33$  ppm where  $3/2 \lambda_{100} = 275$  ppm

and polycrystalline surface has been assumed [26]. On the other hand, for the planes which are perpendicular to the film plane having strong (110) texture,  $\lambda_{\text{eff}}$  can be calculated as  $1/5 \lambda_{100} = 36.66$  ppm. The value we chose is,  $\lambda_{\text{eff}} = 70$  ppm for polycrystalline material.

We chose the value of strain, 400 ppm which can be obtained by applying 2 Kilo-volt along the length of the PMN\_PT (according to plot in figure 2.2.1). The following equations are used for the calculations of the stress and shape anisotropy energies: for the ellipsoidal magnets,

$$\text{Stress Anisotropy Energy: } E_{\text{stress}} = \frac{3}{2} \lambda_{\text{eff}} \sigma * \text{Vol} / \text{eV}$$

$$\text{Shape Anisotropy Energy: } E_{\text{shape}} = 0.5 * \mu * M_{\text{sat}}^2 * \text{Vol} * (N_b - N_a) / \text{eV}$$

, Where,  $\text{Vol} = \text{volume of the magnet} = \frac{\pi}{4} * a * b * c$ ,  $M_{\text{sat}}$  = saturation magnetization, eV = 1 electron volt,  $N_b$  and  $N_a$  are the demagnetization factors along the minor and major axis respectively.

The table 2.2.2 is showing some of the energy calculations based on which we determine the shapes and sizes of the magnets to be used in the study of stress-induced switching. The row designated ‘‘Type’’ shows the aspect ratio. The magnets are elliptical and the entry  $a/b$  implies that the major axis was  $a$  and the minor axis was  $b$ . We have assumed single domain approximation to estimate shape and stress anisotropy energy.

Table 2.2.2 Shape anisotropy, stress anisotropy values of different shapes of nanomagnets

Type (a/b)	300/ 250	290/ 255	320/ 285	270/ 240	250/ 230	240/ 220	200/ 185	220/ 200
<b>Shape Anisotropy (eV)</b>	16	11	11	10	6	6	5	6
<b>Stress Anisotropy (eV)</b>	13	12	15	11	10	9	6	7

The dipole interaction energy between two closely spaced magnets (one more shape anisotropic than the other) has been calculated as follows:

$$E_{dipole} = ((\mu/(4 * \pi)) * M_{sat}^2 * Vol1 * Vol2/r^3)/eV$$

, Where Vol1 and Vol2 are the volumes of highly shape anisotropic and less shape anisotropic magnets. For separation distance of 700 nm between each isolated element of arrays with feature sizes ranging from ~200nm to ~ 330 nm, we estimated the dipole interaction energy as small as 0.8 eV which less than 5% of the shape anisotropic energy. For dipole coupled pairs with separation distance 300 nm, the interaction rises to 10 eV, which is almost 41% of the shape anisotropic energy of nanomagnets with dimensions, 300 nm by 250 nm.

### 2.2.3: Nano-Fabrication with Electron Beam Lithography

A bilayer of positive e-beam resist (495K PMMA and 950K PMMA; 4% Anisole) was spin-coated using the following procedure: A static dispense of ~3 ml (495K PMMA) was carried out on the PMN-PT substrate followed by a dynamic spread at 500 rpm for 5 seconds. The spin cycle was performed by quickly ramping to 2500 rpm and held for 45 seconds. A pre-bake at 115°C (so as not to exceed the PMN-PT Curie temperature of 150°C) was then

performed for 120 seconds, resulting in a 495K PMMA layer of ~ 100 nm. The top 950K PMMA layer was spin-coated next using the same procedure, resulting in the final bilayer PMMA having a thickness of ~ 200 nm. PMMA 495K has higher sensitivity to the electron beam exposure than PMMA 950K. Hence, following the developing procedure, it produces a nice clean undercut as shown in figure 2.2.2. The undercut serves to minimize any side wall deposition on the resist, thus preserving the fine feature sizes of nanomagnets. It is also instrumental for having better lift-off after metal deposition with hot PG-Remove or Acetone.



Figure 2.2.2: Undercut developed for bilayer PPMA resist spun on PMN-PT substrate

The resists are then exposed in a Hitachi SU-70 SEM with a Nability attachment using 30 kV accelerating voltage and 60 pA beam current. Subsequently, the resists were developed in cold MIBK: IPA (1:3) for 90 seconds followed by rinsing in cold IPA for 2 minutes.

#### 2.2.4: Material Deposition and Lift-off

There are several issues with the sputter deposition of FeGa. The sputtering process is conformal, not like directional evaporation. Moreover, the sputtering species are relatively hot which sometimes cure the resist as they impinge on the layer. The pressure for sputtering deposition is another important parameter. The mean free path (MFP) of the energized atoms in the chamber scales with the deposition pressure according to the following equation:

$$MFP \sim 5 * \frac{10^{-3}}{Pressure} cm$$

The typical deposition pressure is 50 mT for DC sputtering. That gives the MFP value roughly 0.1 cm. Our sample to target separation is approximately 5 inch or less. So the atoms undergo many collisions before they hit the substrate. The adatom energy is roughly 1 to 10 eV for sputtering. Therefore, atoms fly around in every direction unlike evaporation and reach the pattern on the substrate from random angles. This eventually causes side wall deposition on the resist and traditionally sputter deposition is good for better side wall coverage. That's why we chose 1 milli-Torr pressure, which results in an MFP of 5 cm. The more the pressure is lowered, the more directional sputtering becomes. Our sputtering instrument is set up for conformal coverage. The following figure shows a schematic of the set up:

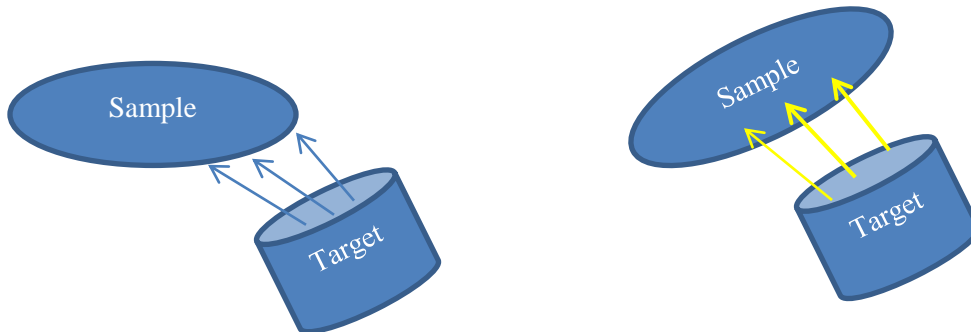


Figure 2.2.3: Schematic picture of sputtering machine and normal deposition on the sample. Therefore, we deposit without rotation of the sample and additionally, care is taken to make the line of sight of the sputtering perpendicular to the sample surface to reduce side wall coverage even more.

For nanomagnet delineation, a 4-5 nm thick Ti layer was first deposited using e-beam evaporation at a base pressure of  $(2-3) \times 10^{-7}$  Torr, followed by the deposition of 10-15 nm of FeGa (thickness verified with AFM) using DC magnetron sputtering of a FeGa target with a base pressure of  $(2-3) \times 10^{-8}$  Torr and deposition pressure of 1 milli-Torr. The magnetron power was 45 W and the deposition was carried out for 33-45 seconds. The nanomagnets were formed following lift-off procedure in hot (60°C) PG-Remover for couple of hours and they were imaged

with both scanning electron microscope (SEM) and atomic force microscope (AFM). Figure 2.2.3 is showing SEM image of nanopatterns on PMN-PT substrate.

### 2.2.5: Magnetic Force Microscopy Imaging of Nanomagnets:

Magnetization states were ascertained with magnetic force microscopy (MFM). All MFM imaging was carried out with a low moment MFM tip in order to perturb the magnetization states of the nanomagnets as little as possible. The nanomagnets are initially magnetized with a large field of 2 Tesla along the nominal direction of the major axis of elliptical shape nanomagnets. This makes the magnetization rotate to nearest easy axis. Then, we perform MFM imaging of the nanomagnets and record the magnetic states of nanomagnets at zero stress. Following first cycle of imaging, a strain of ~400 ppm is applied to the substrate which is mostly transferred to the nanomagnets causing the magnetization to evolve to a new state. Finally, new orientation is captured by second cycle of MFM imaging in order to compare the pre- and post-stress magnetic states of nanomagnets.

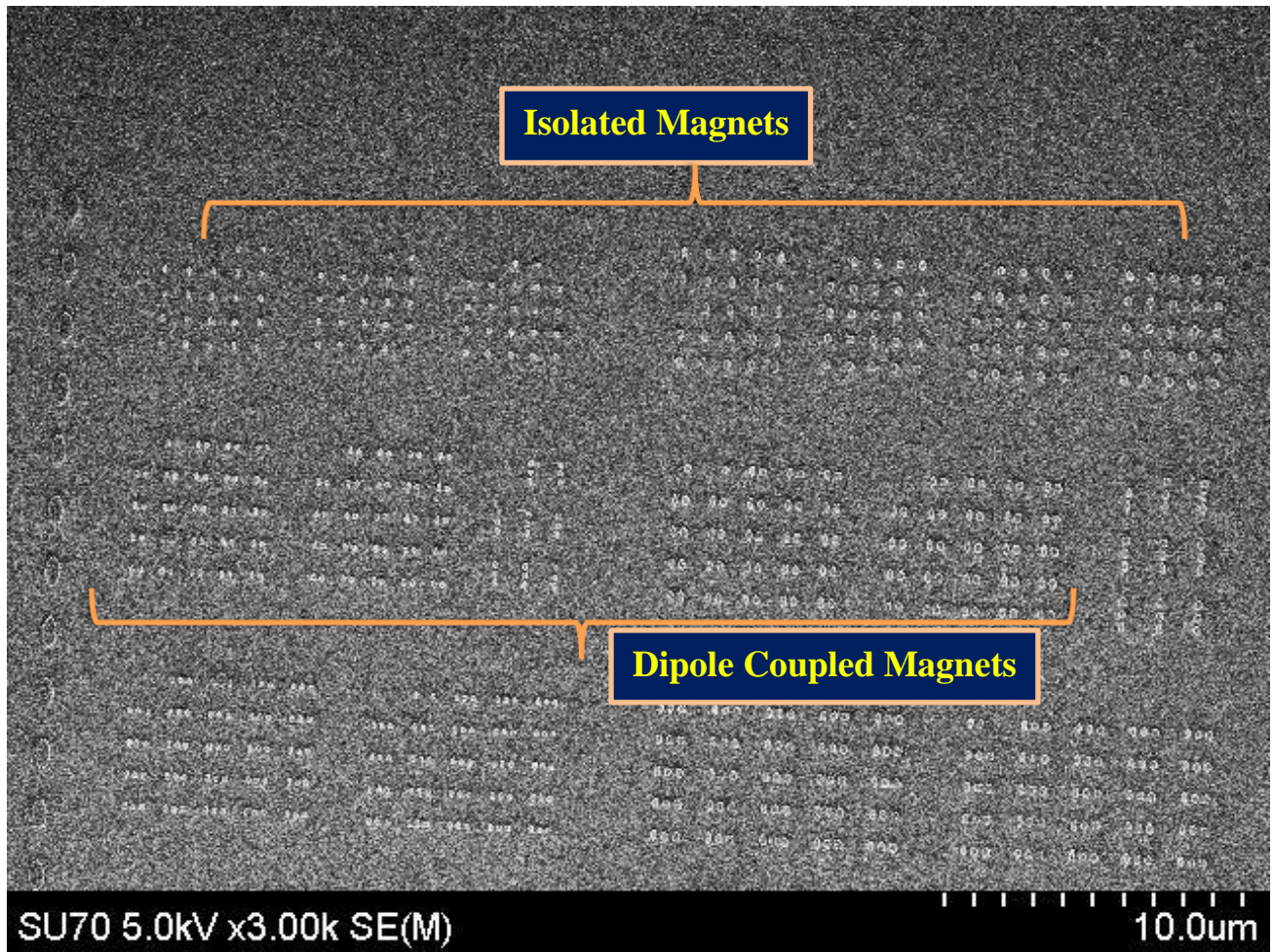


Figure 2.2.4: Scanning electron microscopy image of nanomagnets

## Chapter 3. Demonstration of Electric Field Control of Magnetization Switching in FeGa Nanomagnets

In this chapter, we discuss the experimental results of switching the magnetization states of Galfenol nanomagnets by electric field induced stress. Our system consists of elliptical FeGa nanomagnets of 200–350 nm feature size fabricated on a (100)-oriented PMN-PT substrate (70% PMN and 30% PT) [27]. The fabrication involved electron beam lithography and sputtering. The major axes of the elliptical nanomagnets are aligned nominally parallel to each other on the substrate. Prior to delineation of the nano-magnets, the PMN-PT substrate is poled with an electric field of  $9 \text{ kVcm}^{-1}$  in a direction that will coincide with the major axes of the nanomagnets. Here, we investigate magnetization dynamics of isolated and dipole coupled nanomagnets.

### 3.1: Isolated Nanomagnets

Figure 3.1.1 shows atomic force (AFM) and magnetic force (MFM) micrographs of two nearly elliptical isolated nano-magnets that are placed far enough away from each other to make dipole interaction between them negligible. The MFM shows the in-plane magnetization features. The nanomagnet nominal dimensions are: major axis = 335 nm, minor axis = 286 nm and thickness = 15 nm. Underneath each nanomagnet there is a  $\sim 5$  nm layer of Ti needed to adhere the nanomagnets to the PMN-PT substrate. This layer is thin enough to allow most of the strain generated in the PMN-PT substrate (upon the application of an electric field) to transfer to the FeGa nanomagnets resting on top. The nanomagnets are initially magnetized in one of the

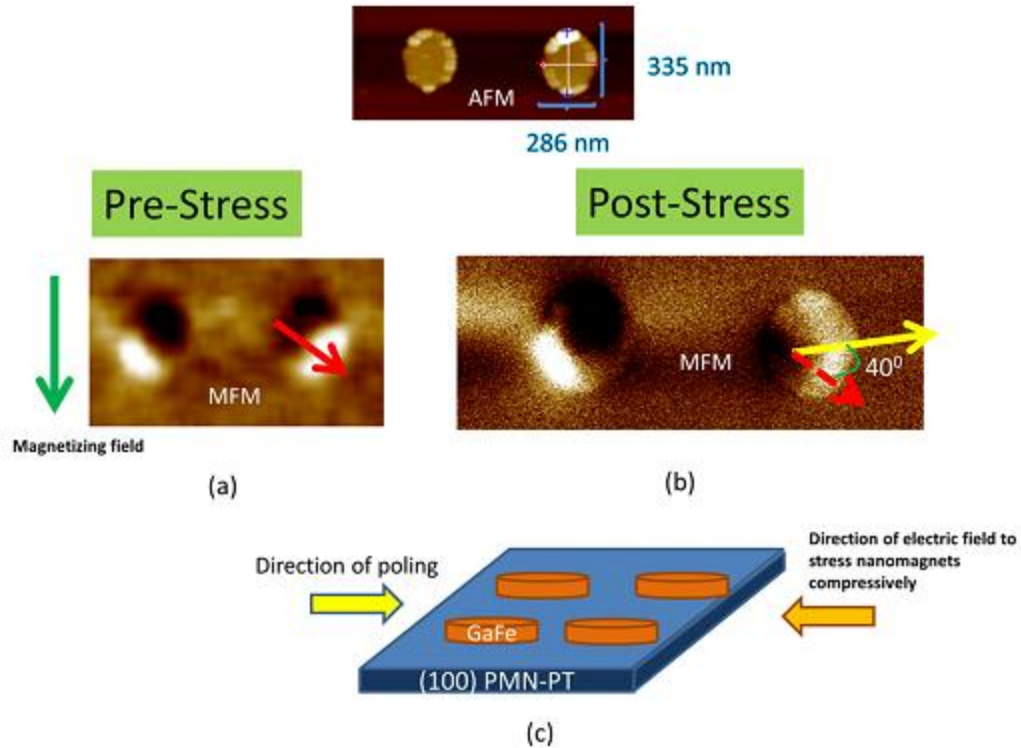


Figure 3.1.1: (a) Magnetic force (MFM) and atomic force (AFM) micrographs of isolated elliptical nanomagnets that have been subjected to a strong magnetic field in the direction indicated by the vertical green arrow. The resulting magnetization direction of the right nanomagnet is indicated by the slanted red arrow. (b) The MFM image of the nanomagnets after they have been stressed with an electric field and relaxed (stress withdrawn). The magnetization direction of the left nanomagnet does not show any discernible change, but the right nanomagnet's magnetization has rotated to a new orientation shown by the slanted solid yellow arrow. For comparison, the initial orientation of this nanomagnet's magnetization is shown by the broken red arrow. The magnetization has rotated by  $\sim 40^\circ$  owing to the stress generated by the electric field and subsequent removal of the electric field has not returned the magnetization to the original state, but left it in the new state. (c) The poling direction and direction of electric field applied to generate compressive stress along the nominal major axes of the nanomagnets.

two directions along their major axes with a 1.5 T magnetic field as shown by the vertical green arrow in figure 3.1.1(a). The MFM image in figure 3.1.1(a) shows that after the magnetizing field has been removed, the nanomagnets have close to a single-domain state with their magnetizations pointing not quite along that of the applied magnetic field, but reasonably close to it. The deviation could be due to lithography imperfections (see the AFM images) that make the shapes of the nanomagnets slightly non-elliptical (which is why the stable orientation is not

exactly along the major axis) or the presence of pinning that pins the magnetization in an orientation subtending a small angle with the major axis. An electric field of  $4.2 \text{ kV cm}^{-1}$  is then applied across the PMN-PT substrate in the direction opposite to the poling direction to generate compressive stress along the nano-magnets' major axes (see figure 3.1.1(c)). This field is generated by applying a voltage of 2.1 kV across a 5 mm long substrate and this voltage is within the linear strain-versus-voltage regime determined in [19]. This field strains the PMN-PT substrate owing to  $d_{33}$  coupling. The value of  $d_{33}$  measured in our substrates in [19] was  $1000 \text{ pm V}^{-1}$ . Therefore, the average strain generated in the PMN-PT substrate is 420 ppm. If all of it is transferred to the FeGa nanomagnets, then the stress generated in them is  $\sim 33 \text{ MPa}$  since the Young's modulus of FeGa is about 75 GPa. The nanomagnets are compressed in the direction of their major axes by the electric field and since FeGa has a positive magnetostriction, this should rotate the magnetization of the magnetized nanomagnets toward the minor axis because stress anisotropy relocates the potential energy minimum to an orientation that is perpendicular to the stress axis. It is expected that after the electric field (or stress) is removed, the magnetization will return to the original orientation, or perhaps to some other orientation, since the potential energy landscape changes when stress is withdrawn.

From figure 3.1.1 (b) illustrates the post-stress magnetization states. The left nanomagnet's magnetization is indeed in the original orientation but the right nanomagnet's magnetization is not. The left's magnetization is in the original orientation because it either did not rotate at all (perhaps owing to the fact that the stress generated in it was insufficient to overcome the shape anisotropy energy barrier in this nanomagnet and make its magnetization rotate, or the magnetization was pinned by defects) or it did rotate but returned to the original orientation after the removal of stress, as expected. What is interesting is that the right

nanomagnet's magnetization has assumed an orientation subtending an angle of  $\sim 40^\circ$  with the original. Clearly, in this nanomagnet, stress was able to overcome the shape anisotropy energy barrier and budge the magnetization from its original orientation, but after stress withdrawal, the magnetization settled into a different orientation and stayed there. This is obviously a metastable orientation corresponding to a local potential minimum that is robust against thermal noise and could have arisen either because the shape of the right nanomagnet deviates significantly from elliptical causing local minima to appear in the potential profile of the nanomagnet, or pinning sites pin the magnetization in a given state after stress withdrawal, or there are multiple phases (or even multiple chemical constitution owing to some surface oxidation) that lead to multiple coercivities [28] associated with the presence of multiple energy barriers in the potential profile separated by local energy minima. The stress anisotropy gives rise to an effective magnetic field given by  $H_{eff} = 3/2 |\lambda_s| \sigma / (\mu_0 M_s)$ , where  $\lambda_s$  is the magnetostriction coefficient,  $\sigma$  is the stress,  $\mu_0$  is the permeability of free space and  $M_s$  is the saturation magnetization of the nanomagnet. If the material has two different coercivities  $H_1$  and  $H_2$ , and the inequality  $H_1 < H_{eff} < H_2$  holds, then stress can get the magnetization stuck in a metastable state.

There can be another feature peculiar to FeGa alloys. A recent paper suggests that there is significant non-Joulian magnetostriction in FeGa alloys [22] which can complicate the stress induced magnetization rotation process in this material and perhaps drive the magnetization to metastable states. To ascertain that this effect is repeatable, we examined another set of nanomagnets of slightly different dimensions (major axis = 337 nm, minor axis = 280 nm and thickness = 16 nm). The corresponding AFM and MFM pictures are shown in figure 3.1.2.

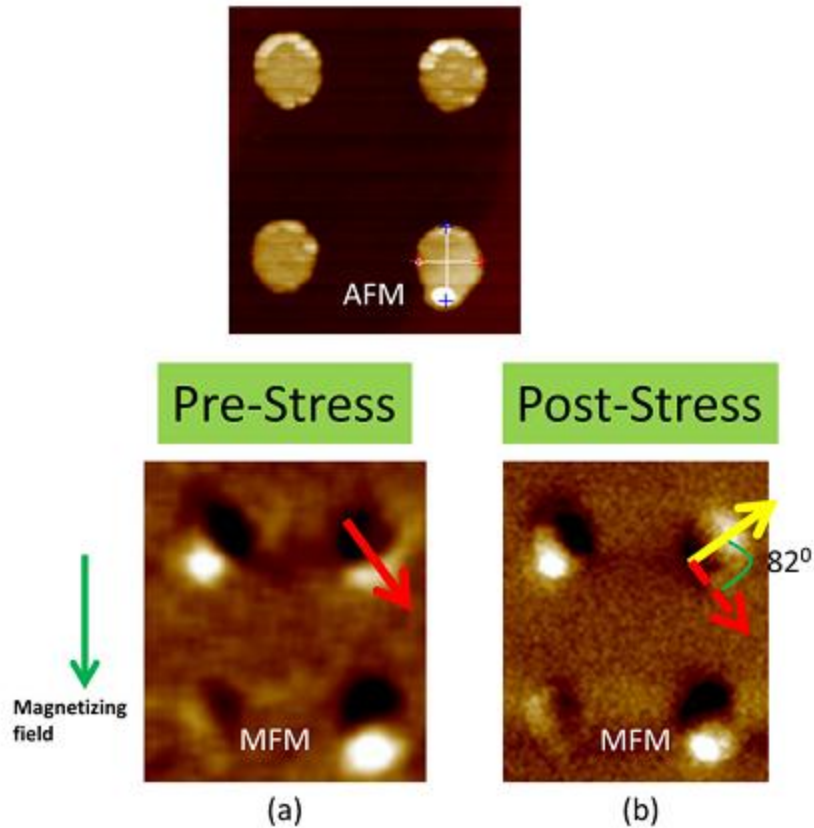


Figure 3.1.2: (a) Same as figure 1(a), except there are four nanomagnets in this image. The initial magnetization direction of the nanomagnet in the upper right corner is indicated by the slanted red arrow. (b) MFM image after application and removal of stress. The magnetizations of all nanomagnets except the one in the upper right corner show no discernible difference between the pre- and post-stress conditions, but the magnetization of the one in the upper right corner has rotated by  $\sim 82^\circ$ . Notice that this nanomagnet is most ‘circular’ of all and therefore has the lowest shape anisotropy energy barrier, which is why stress was able to rotate its magnetization.

The three nanomagnets (among the four shown) that have the highest shape anisotropy (highest eccentricity of the ellipse) do not show any perceptible difference between the pre- and post-stress magnetization states (either because their magnetizations did not rotate when stressed or returned to the original states after stress removal), but the least shape anisotropic nanomagnet has evolved to a different state after stress removal. The new state’s magnetization has an angular separation of  $\sim 82^\circ$  from the original magnetization state. Once again, the new state is non-volatile. Altering the magnetization state of a magnet with an electric field is the converse

magnetoelectric effect. Therefore, we have observed clear evidence of the converse magnetoelectric effect in the nanoscale and the effect has the property of non-volatility.

### 3.2: Dipole Coupled Nanomagnets

In order to investigate whether this effect is influenced by dipole coupling between nanomagnets, we fabricated arrays of closely spaced nanomagnet pairs whose mutual separations are small enough to allow reasonable dipole coupling between them. One nanomagnet in the pair is intentionally made much more shape anisotropic than the other. This makes the former magnetically stiff (or hard) and its magnetization cannot be budged by the stress generated because of the extremely high shape anisotropy energy barrier. The latter has much less shape anisotropy and hence is softer. Its magnetization state can be affected by stress.

Figure 3.2.1 shows the pre-stress MFM images of four such pairs which have all been initially magnetized with a strong magnetic field, making their magnetizations approximately parallel. Dipole coupling would prefer anti-parallel ordering within a pair, but the dipole coupling strength is insufficient to overcome the shape anisotropy energy barrier of any soft magnet to rotate its magnetization and make the two magnetization orientations in a pair mutually anti-parallel after the magnetizing field has been removed. Next, all nanomagnets are compressed along their nominal major axes with an electric field and the field is withdrawn. Figure 3(b) shows the post-stress MFM images. Three pairs show no perceptible difference between the initial and final orientations, but the fourth pair in the upper right-hand corner shows that the magnetization of the soft nanomagnet has rotated by a larger angle of  $110^\circ$  ( $> 90^\circ$ ) and once again the new state is non-volatile. The larger angle of rotation (compared to the case of isolated nanomagnets) is obviously due to dipole coupling.

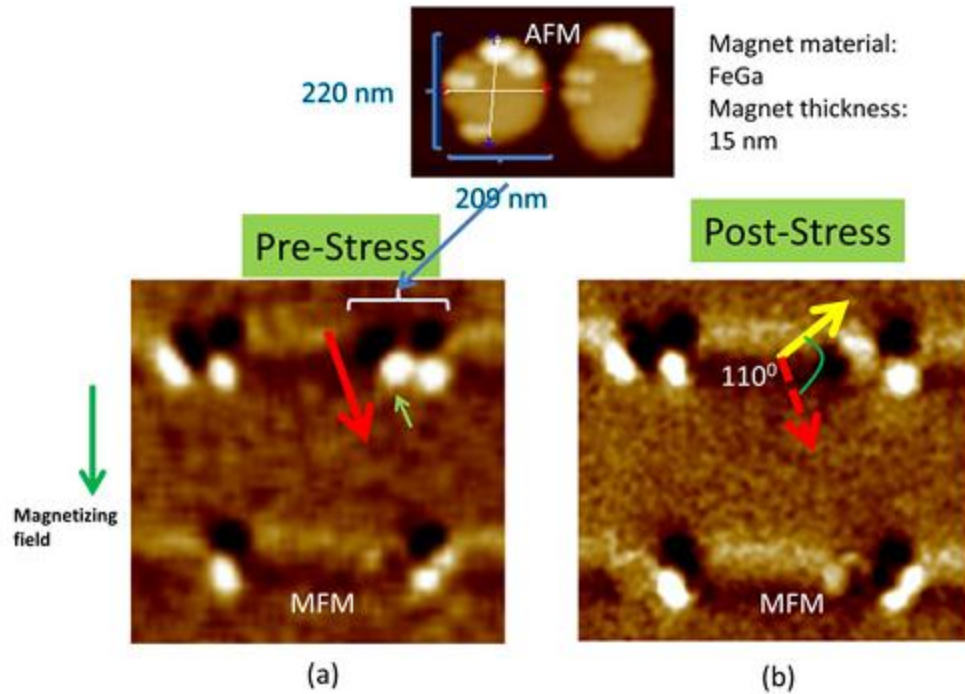


Figure 3.2.1: Dipole-coupled pairs where the right partner is much more shape anisotropic than the left partner, making the right partner hard and the left partner soft. (a) MFM image after being magnetized by a magnetic field in the direction of the green vertical arrow and before application of stress. (b) MFM image after application and removal of stress. The magnetizations of all pairs, except the one in the upper right corner, show no discernible difference between the pre- and post-stress conditions, but the magnetization of the soft nanomagnet in the upper right corner (indicated by the short light green arrow) has rotated by  $\sim 110^\circ$ .

The latter prefers anti-ferromagnetic ordering within a pair, i.e., the magnetization of the soft nanomagnet should be anti-parallel to that of the hard nanomagnet. This is not completely achieved because the magnetization ultimately gets trapped in a metastable state, but it does not get trapped in a metastable state that is close to the original state because the dipole coupling is strong enough to dislodge the magnetization from any such state and steer it to a state subtending a large angle with the original state. The difference between the isolated and dipole-coupled cases is that in the former, the angular separation between the old and new states is less than  $90^\circ$ ,

whereas in the latter, it is greater than  $90^\circ$ . Therefore, the converse magnetolectric effect is influenced by dipole coupling.

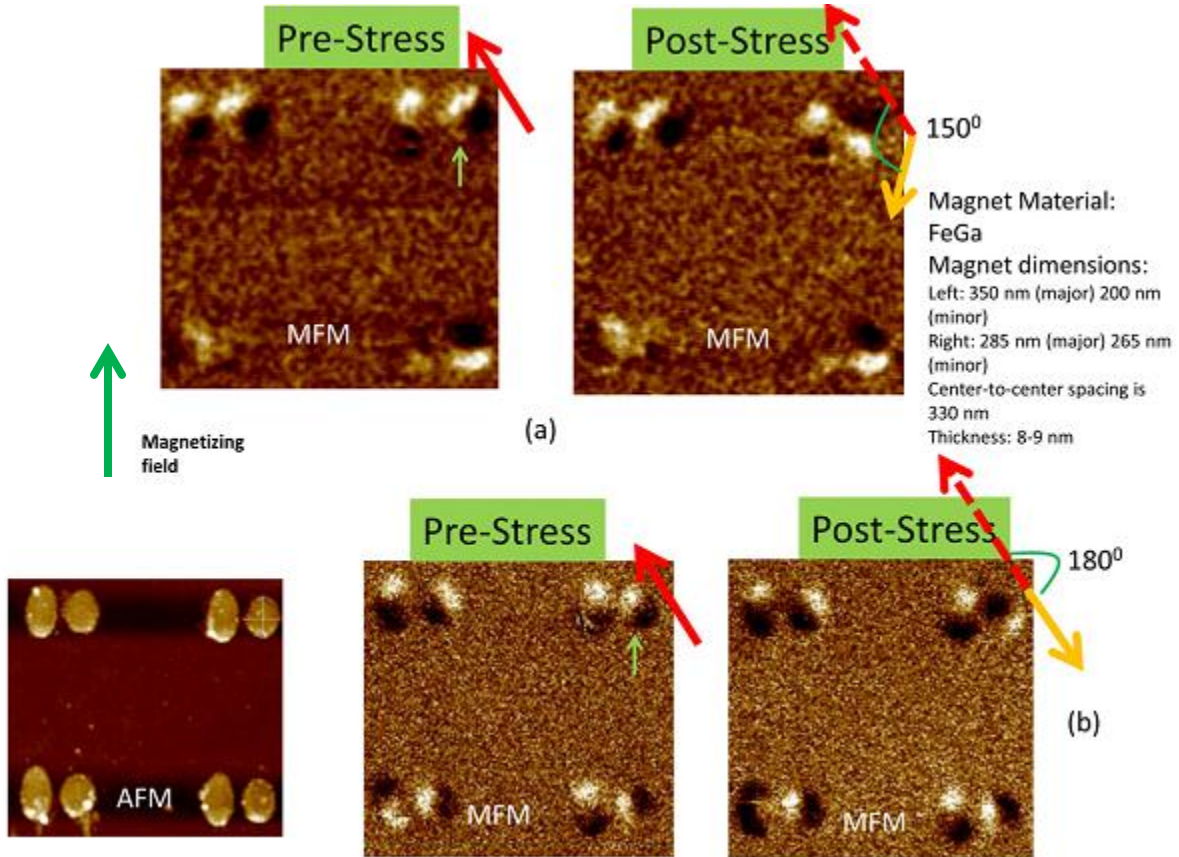


Figure 3.2.2: (a) MFM image of a dipole-coupled pair after being magnetized by a magnetic field in the direction of the green vertical arrow and before application of stress is shown on the left. In these pairs, the left partner is more shape-anisotropic than the right, i.e., the left nanomagnet is ‘hard’ and the right nanomagnet is ‘soft’. MFM image after application and removal of stress is shown on the right. The magnetizations of all expect the pair in the upper right corner show no discernible difference between the pre- and post-stress conditions, but the magnetization of the soft nanomagnet in the upper right corner (indicated by the short light green arrow) has rotated by  $\sim 150^\circ$ . (b) Similar to (a), except now the rotation is by  $180^\circ$ .

In figure 3.2.2, we show two more dipole coupled pairs, initially magnetized in the same direction, where the magnetization of the soft nanomagnet has rotated by  $\sim 150^\circ$  in one case, and  $\sim 180^\circ$  in the other case, after application and withdrawal of stress. Once again the dipole

coupling, which prefers anti-parallel magnetizations of the two magnets, is responsible for the  $> 90^\circ$  rotation of the magnetization.

### 3.3: Implementation of NOT Logic gate or Inverter:

The above mentioned results not only show that electric field control of local magnetization orientation (and hence local magnetic field) is possible, but also that the effect is nonvolatile and can be influenced by neighboring magnetization states because of dipole coupling. This influence is critical to implement the conditional dynamics of Boolean (or even non-Boolean) logic where the state of one logic device determines the state of the next. The dipole-coupled pair, for example, acts as an inverter (NOT gate) Let the hard (more shape anisotropic) nanomagnet host the input bit and the soft (less shape anisotropic) nanomagnet the output bit. Let us say that we encode the logic bit '1' in the initial magnetization orientation of both magnets (which are made mutually parallel by the magnetizing field). The input bit then becomes '1'. The application of the electric field acts like a clock signal that triggers the output bit to become 'not 1' (because the magnetization rotates by a large angle from the initial orientation), which we designate as bit '0'. This results in successful inversion and a clocked NOT gate.

Finally, because the magnetization rotation is non-volatile, there are also potential applications in non-volatile memory where bits, encoded in the magnetization orientation, are written with a voltage. Because of the extremely low energy dissipation in electric field control of magnetization [10], [17], [28], [29], these initial observations are encouraging for future energy-efficient nanomagnetic computing.

## **Chapter 4. Reversible Strain-induced Magnetization Switching in FeGa Nanomagnets- A Scheme to Realize Straintronic Memory Cell**

In chapter 4, we will illustrate the core component of a straintronic non-volatile, rewritable, non-toggle memory element using Galfenol nanomagnet. As mentioned before, a nanomagnet can store bits of information (typically ‘1’/ ‘0’) in a stable or metastable magnetization state. Writing a bit involves switching the magnetization to the desired state by an external agent. There are two most desirable properties while employing any writing scheme. First, the process should be minimally dissipative. Second, the writing agent should not have to read the earlier stored bit first and then decide on a course of action to write the desired bit based on that knowledge. The latter is known as the non-toggle behavior of a memory. In a non-toggle memory the writing agent can write either bit deterministically without needing to know what the previously stored bit was.

### **4.1: Background and Experimental Setup**

Spin transfer torque, domain wall motion or uses of giant spin hall effect to generate spin polarized current are all regrettably energy hungry and consume energy between  $10^4$  kT to  $10^7$  kT. The multiferroic nanomagnet studied in this research employing thin magnetostrictive nanomagnet coupled to a piezoelectric substrate, can come to the rescue by reducing energy dissipation to 2 or 3 orders of magnitude less than conventional transistors that dissipate at least  $\sim 10^4$  kT of energy to switch in isolation. Non-toggle writing schemes based on such strain-induced switching of a magnetostrictive nanomagnet from one stable state to another have been proposed in the past [28], [30].

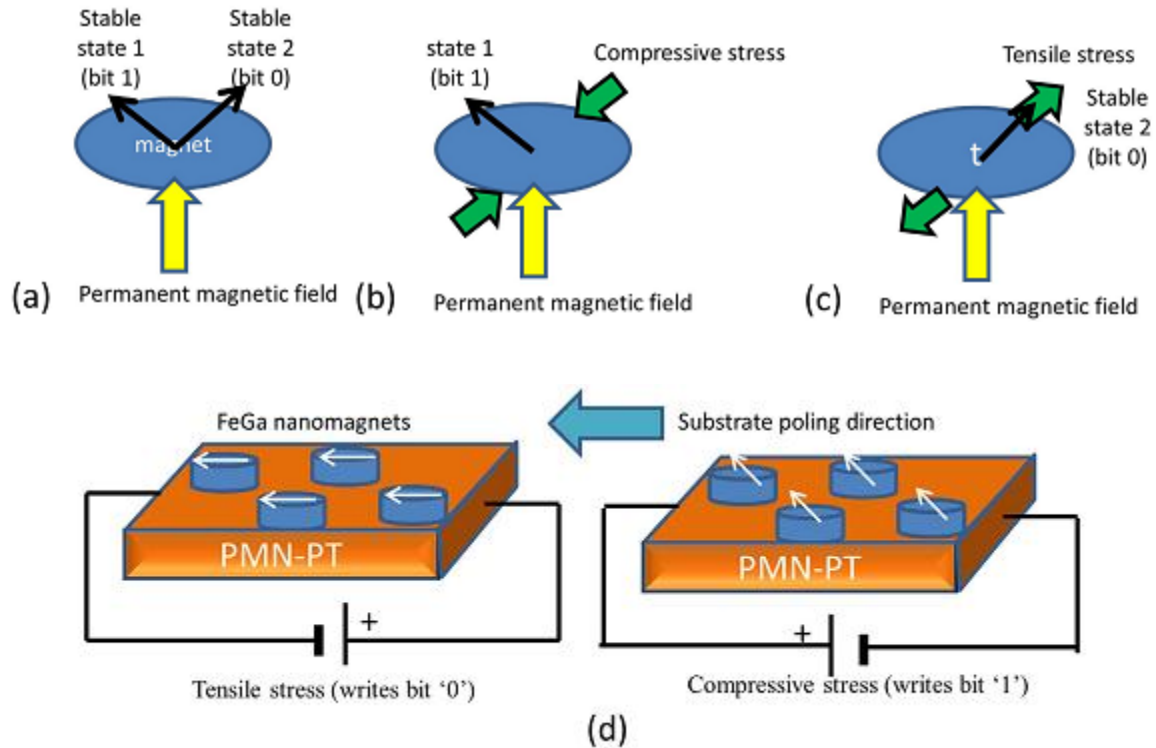


Figure 4.1: (a–c) Non-toggle straintronic memory of the type discussed in refs 10,11. (a) A magnetic field applied along the minor axis of an elliptical nanomagnet gives rise to two stable magnetization orientations at an angle with each other (the angle depends on the magnetic field strength, shape of the nanomagnet, etc.). They encode bits ‘0’ and ‘1’. (b) We will assume that the magnetostriction coefficient of the nanomagnet is positive. Then, compressive stress along an axis collinear with one stable state (say, state 2) causes the magnetization to settle into state 1. If the magnetostriction coefficient were negative, the magnetization would have settled into state 2. (c) Tensile stress along the same axis causes the magnetization to settle into state 2 for positive magnetostriction and state 1 for negative magnetostriction. Therefore, we can write either bit by choosing the sign of the stress along the stress axis. We do not need to know what the previously stored bit was in order to write the desired bit. (d) Our test set-up. Electric field in the direction of substrate poling generates tensile stress in the nanomagnets whose major axes are aligned collinear with the poling direction. This aligns the magnetizations along one direction and writes bit ‘0’. Electric field in the opposite direction generates compressive stress and aligns the magnetizations in a different direction, writing bit ‘1’.

Electrostatic potential of one polarity generates compressive strain in the nanomagnet and switches the magnetization to one state (to write bit ‘0’) and voltage of the opposite polarity generates tensile strain and switches the magnetization to the other state (to write bit ‘1’). This is illustrated in Fig. 4.1(a–c). According to theoretical calculations, roughly 850 kT of energy will

be dissipated to write a bit in  $\sim 1.5$  ns at room temperature in this type of non-toggle memory [28].

Our system consists of Elliptical FeGa nanomagnets of major axis  $\sim 300$  nm, minor axis  $\sim 240$  nm, and thickness  $\sim 8$  nm were fabricated on a (100)-oriented PMN-PT substrate (70% PMN and 30% PT) [31]. The substrate was first poled with an electric field of 8400 V/cm in a direction which will coincide with the major axes of the nanomagnets (the major axes of the nanomagnets were nominally parallel to each other) prior to fabrication of the nanomagnets. In order to study magnetization switching, we first magnetized all FeGa nanomagnets on a PMN-PT wafer with a  $\sim 2$  Tesla magnetic field directed along the nominal major axis of the nanomagnets. The magnetization states of nanomagnets were then determined with magnetic force microscopy (MFM). Care was taken to use low-moment tips in order to not perturb the magnetization states of the nanomagnets with the tip.

## 4.2: MFM imaging of First Cycle of Compressive and Tensile Stress

Vertical panel 2 of figure 4.2.1 and figure 4.2.2, show that most nanomagnets have been magnetized in the direction of the field, but some have been magnetized in an orientation that subtends a non-zero angle with the magnetizing field. This odd behavior is ascribed to the presence of spurious energy minima in the potential profile of these nanomagnets in a magnetic field that are caused by either the presence of multiple energy barriers due to irregular shapes, or multiple phases, or pinning sites. The magnetic field drives a nanomagnet to an energy minimum closest to the initial state, whose magnetization orientation may not be collinear with the field.

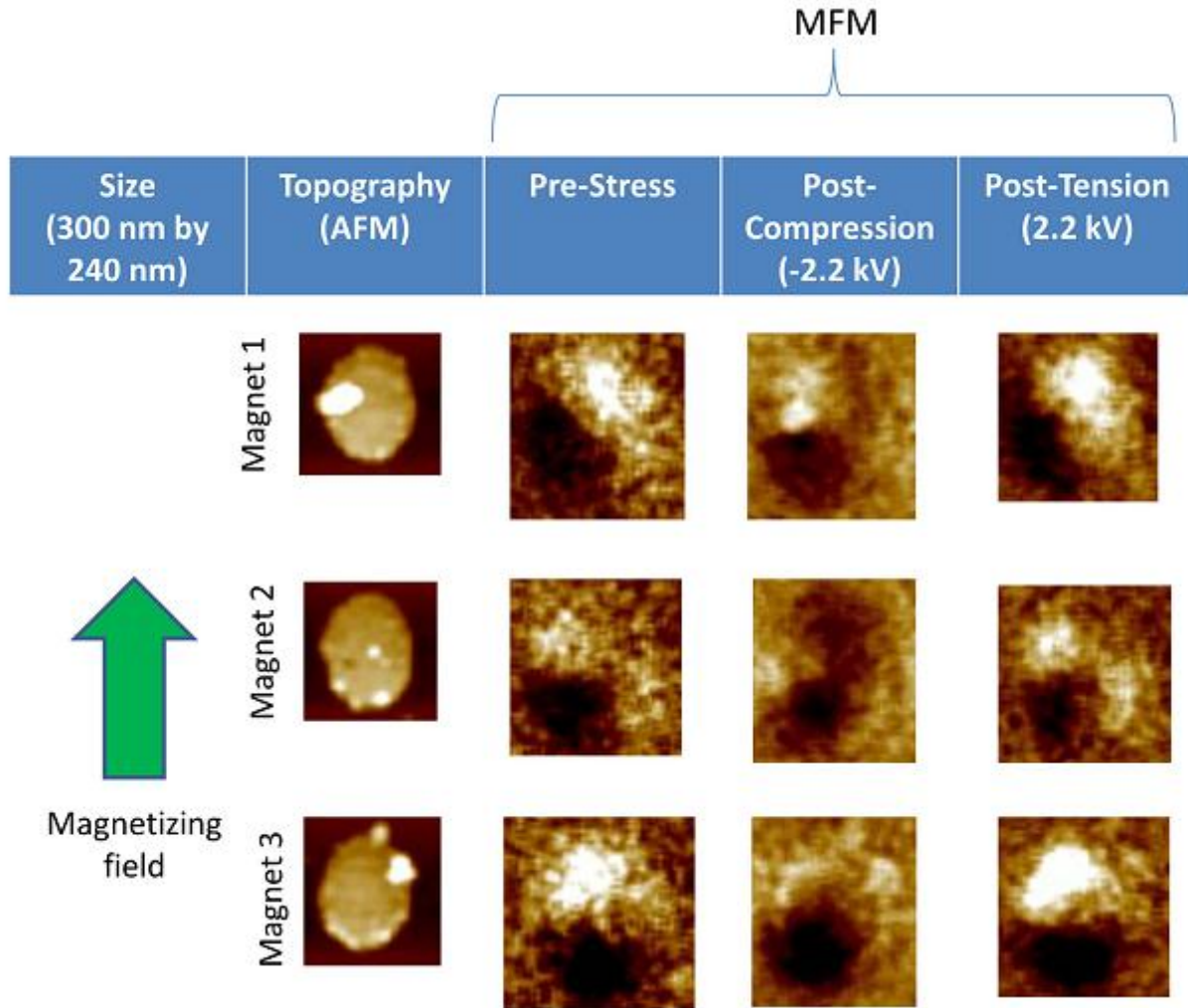


Figure 4.2.1: Magnetic force (MFM) and atomic force (AFM) micrographs of three isolated elliptical FeGa nanomagnets that have all been magnetized with a magnetic field in the direction indicated by the thick vertical green arrow. Starting from the left, the first vertical panel shows the AFM image of the nanomagnet, the second vertical panel shows the initial magnetization state after magnetizing with the field (note that the magnetization is not always in the direction of the field), the third vertical panel shows the new magnetization state after compressive stress is applied and withdrawn, and the last vertical panel shows the magnetization state after tensile state is applied and withdrawn. Note that compressive stress takes the magnetization to a state different from the initial one and keeps it there after stress withdrawal (non-volatile). Tensile stress brings it back to the original state and keeps it there after stress withdrawal. Thus, tensile stress always writes the bit '0' and compressive stress writes a bit that is 'not-0' and we call it bit '1'. This realizes a non-volatile, non-toggle memory.

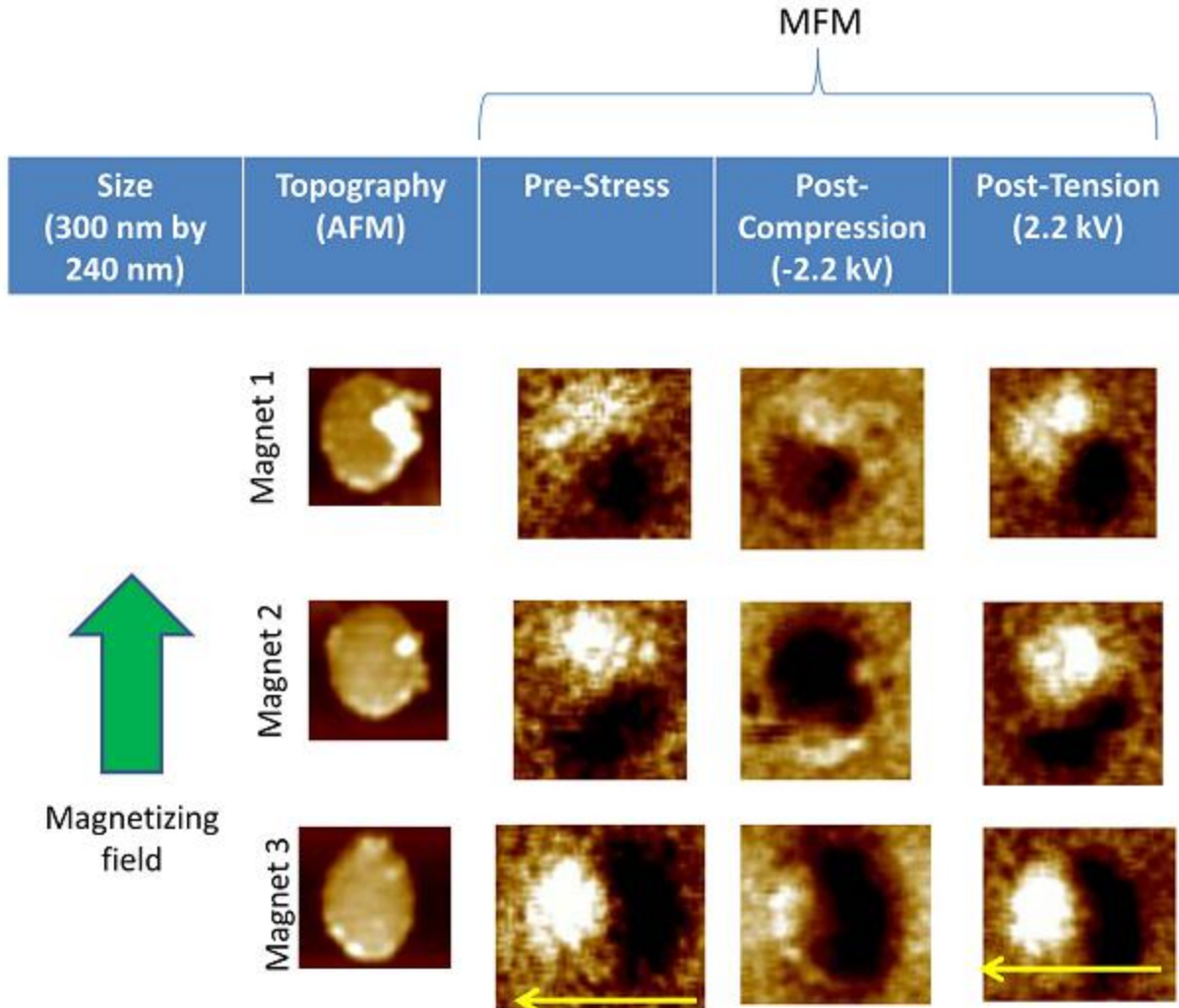


Figure 4.2.2: Same as figure 4.2.1, but for a different set of nanomagnets. Here, the nanomagnet in the last row was magnetized in a direction almost perpendicular to the magnetizing field showing that there is a deep energy minimum corresponding to that orientation and the nanomagnet prefers to go there even in the presence of the magnetizing field. Compressive stress, however, seems to drive it out of that state, but subsequent application of tensile stress brings it back to that state, just like in the case of the other nanomagnets. Again, a non-volatile, non-toggle memory is implemented.

After the initial magnetizing, every nanomagnet is compressively stressed along its major axis by subjecting the PMN-PT substrate to a global average electric field of 4.4 kV/cm in a direction opposite to that of the initial poling (see Figure 4.1(d)). The field is generated by applying a potential of  $-2.2$  kV along a 5 mm long substrate. It strains the PMN-PT substrate owing to  $d_{33}$  coupling. The value of  $d_{33}$  measured in our substrates in ref. [1] was 1000 pm/V.

Therefore, the average strain generated in the PMN-PT substrate is 440 ppm. This strain is partially or completely transferred to the FeGa nanomagnets, resulting in a maximum stress of ~33 MPa in the nanomagnets since the Young's modulus of FeGa is about 75 GPa [32]. The electric field lines in the vicinity of the nanomagnets are not necessarily directed along the major axes because of fringing effects and the stress on a nanomagnet is not necessarily uniaxial along the major axis. However, the exact field or stress distribution in space is not important; in the end, the average stress generated in a nanomagnet is either compressive or tensile depending on the polarity of the voltage. This compression or tension alters the magnetization states.

Compressive stress makes the magnetization evolve to a new state, and the magnetization stays there after the stress (electric field) is removed, showing that the new state is “non-volatile”. This is shown in the third vertical panels of Figure 4.2.1 and 4.2.2. Next, tensile stress is applied along the major axis of the nanomagnets by reversing the polarity of the voltage from  $-2.2$  kV to  $+2.2$  kV. The fourth vertical panels of Figure 4.2.1 and 4.2.2 show that all nanomagnets that were imaged returned to the original state after experiencing tension (it is possible, however, that some nanomagnets that were not imaged failed to return to their original states). All this shows two important features: First, one can “rewrite” a bit in the nanomagnets after the first writing (rewritable non-volatile memory), and second, the switching is “non-toggle”. Writing does not always require toggling the previously stored bit; if we apply a positive voltage and tensile stress, then we will always deterministically write the bit 1 irrespective of whether the previously stored bit was 1 (no toggling required) or 0 (toggling required). The same is true if we wish to write the bit 0. In fact, we do not even need to know what the previously stored bit was, which avoids a read step.

### 4.3: MFM imaging of Second Cycle of Compressive and Tensile Stress

In Figure 4.3, we show magnetic force micrographs of three FeGa nanomagnets to establish that the stress-induced magnetization switching between two distinct states is repeatable. In successive vertical panels, we present the initial magnetization state, the state after the first compression cycle, the state after the first tension cycle, the state after the second compression cycle, and the state after the second tension cycle. In the nanomagnets that switch, compression always drives the magnetization away from its pre-stress state and tension always brings it back to the pre-stress state. Unfortunately, we cannot cycle the stress too many times to assess the endurance since the piezoelectric substrate develops fatigue and physically cracks after a few cycles. Our substrate is sourced from a commercial vendor and not of the quality of thin films. Unclamped thin films grown on high quality substrates [14] will presumably be less prone to fatigue and exhibit better behavior. Although, we cannot test the endurance, we note that the effect is perfectly repeatable and is seen in every nanomagnet that shows the switching behavior. We show the MFM images for three arbitrarily chosen nanomagnets and all three exhibit this feature.

One important observation is that the state under tension is unique, but the state under compression is not. At different times, compression drives the magnetization to different states. This is not surprising in a multi-phase ferromagnet where there will be multiple metastable states and different ones can be accessed at different times when the nanomagnet is compressed. Which of these states is visited under compression is not controllable, but what is important is that the

visited state is always distinct from the state visited under tension. For memory applications that is sufficient.

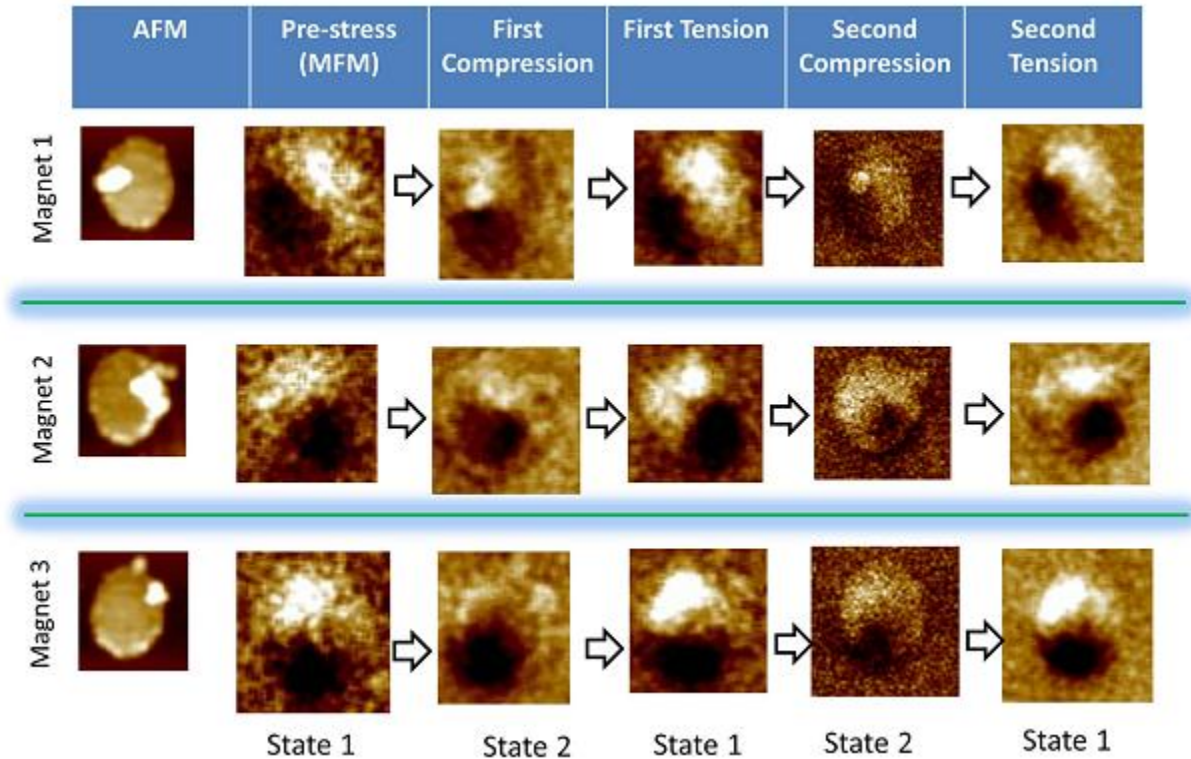


Figure 4.3: Magnetic force microscope images of nanomagnets showing repeatability of the switching. A nanomagnet cycles through its two magnetization states repeatedly with successive compression and tension. Whenever the stress is tensile, the magnetization goes into one state and whenever stress is compressive, it goes into the other state. This consistency shows that the memory has endurance.

#### 4.4: Implementation in a Straintronic Memory Scheme:

We could fashion a memory element by using a magneto-tunneling junction (MTJ) with a FeGa soft layer and magnetize the hard layer permanently in a direction anti-parallel to the pre-stress magnetization orientation of the soft layer. Then, tensile stress applied with one voltage polarity will always take the MTJ resistance to a high state (encoding, say, bit 1) and

compressive stress applied with the other voltage polarity will take the MTJ resistance to a different state encoding the logic complement of the bit 1.

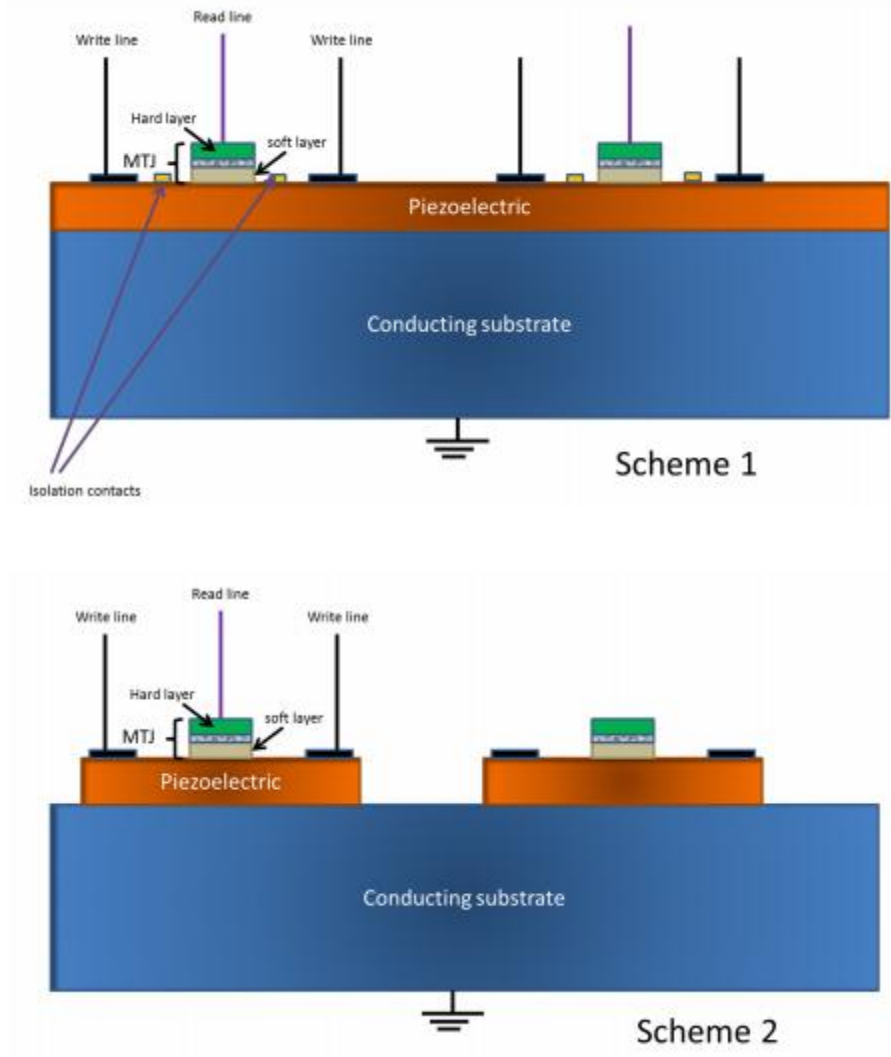


Figure 4.4: A straintronic memory array compatible with a crossbar architecture. Not drawn to scale.

Figure 4.4 shows two possible implementations of a memory array. In the first scheme, we have a continuous piezoelectric thin film and strain is localized around each nanomagnet with isolation gate pads in the manner of ref. [33]. In the second scheme, the piezoelectric layer is mesa-etched and a nanomagnet is delineated on top of each mesa. Since strain exists only in the

piezoelectric material, this strategy provides automatic strain (and hence bit) isolation. The isolation gate pads are not repeatedly charged and discharged during reading/writing of bits and hence do not dissipate energy. We follow the scheme of [14] for generating the necessary strain around each nanomagnet. The two write lines will be shorted together and a potential will be applied between them and the grounded substrate. This potential is dropped across the piezoelectric layer since the substrate is conducting. The magnitude of this potential is the product of the electric field needed to write a bit and the thickness of the piezoelectric layer, which is  $\sim 100$  nm. This potential is a few tens of mV. The piezoelectric layer is poled in the vertical direction. Because of  $d_{33}$  and  $d_{31}$  coupling, the applied voltage generates biaxial strain around the nanomagnets [14]. For one polarity of the voltage, there will be compression along the major axis and tension along the minor axis, whereas for the other polarity, the signs of the strain will be reversed. Thus one voltage polarity will write bit '0' and the other will write bit 'not 0' or, equivalently, bit '1' into the resistance state of the MTJ. For reading, the write lines are grounded so that there is no voltage over the piezoelectric and the MTJ resistance between the read line and the grounded write lines is read to determine if the stored bit is 0 or 1.

## 4.5 Energy Calculation

Consider the memory array shown in the figure 4.4. If strain is generated in a nano magnet in the manner of, say, ref. [14], then a voltage will be applied between the top contacts and the grounded substrate to strain the nanomagnets. In that case, the electric field of 4.4 kV/cm will appear across the thickness of a  $\sim 100$  nm piezoelectric layer, resulting in a switching voltage  $V$  of only  $4.4 \text{ kV/cm} \times 100 \text{ nm} = 44 \text{ mV}$ . This method generates biaxial strain (tension along the minor axis of the elliptical nanomagnets and compression along the major axis, or vice versa,

depending on the voltage polarity which is even better because it results in larger stress anisotropy energy. This may further reduce the voltage (and electric field) needed to rotate magnetization and therefore further reduce the energy dissipation.

For an effective electrode area of  $100 \text{ nm} \times 100 \text{ nm}$  and a piezoelectric film thickness of  $100 \text{ nm}$ , the electrode capacitance in the scheme of 24 would be  $\sim 2 \times 1000 \times 8.854 \times 10^{-12} \times 100 \text{ nm} \times 100 \text{ nm} / 100 \text{ nm} = 1.7 \text{ fF}$  (there are two electrodes that are shorted in the scheme of 24). The resulting energy dissipation  $\sim CV^2$  to write a bit would have been only  $1.7 \text{ fF} \times (0.044 \text{ V})^2 = 3.3 \text{ aJ}$  (788 kT at room temperature). There is also some internal energy dissipation in the nanomagnet owing to Gilbert damping, but that is on the order of  $1 \text{ aJ}$  [34]. If we add that, the total dissipation would be  $\sim 4.3 \text{ aJ}$  (1027 kT). In contrast, present day mainstream spin-transfer torque random access memory (STT-RAM) dissipates about  $10^7 \text{ kT}$  of energy per write operation [8] and spin-Hall based versions will dissipate  $\sim 10^4 \text{ kT}$ .

In conclusion, we have demonstrated the core component of a straintronic non-volatile, rewritable, non-toggle memory element. Since the magnetization switching is induced by strain, it should be remarkably energy-efficient going by all available theoretical predictions. Therefore, this experiment lays the foundation of a remarkably energy-efficient non-toggle non-volatile straintronic memory technology.

## Chapter 5. Repeatable $\sim 180^\circ$ Switching of Magnetization of Nanomagnets by Localized Strain

Magnetic random access memory (MRAM) is generally composed of a magnetotunneling junction (MTJ). An MTJ consists of a hard and a soft ferromagnetic layer separated by a spacer that acts as a tunnel barrier. The soft layer is shaped like an elliptical disk that has two stable (mutually anti-parallel) magnetization states along its major axis. The hard layer is permanently magnetized parallel to one of those states. When the soft layer's magnetization is parallel to that of the hard layer, the MTJ's resistance is low and encodes one binary bit (say '0'), and when it is anti-parallel, the MTJ's resistance is high and encodes the other bit (say '1'). If we employ voltage-generated uniaxial strain/stress to rotate the magnetization of the soft layer to write a bit, we can achieve unprecedented energy efficiency [13]. Unfortunately, strain/stress can rotate the magnetization of a nanomagnet by only up to  $\sim 90^\circ$ . After the withdrawal of stress, the final magnetization state will have roughly equal likelihood of returning to the original stable orientation (not flipping, or  $0^\circ$  rotation) or flipping to the other stable orientation ( $180^\circ$  rotation). That makes the flipping only  $\sim 50\%$  likely, which is undesirable. However, if the stress is withdrawn precisely at the moment when the magnetization has rotated through  $90^\circ$  from the original orientation, then a residual torque due to the magnetization vector's out of plane component may continue to rotate it beyond  $90^\circ$  and achieve a "flip" with very high probability ( $> 99.99\%$  at room temperature)<sup>10</sup>. To achieve this, we require a feedback mechanism that will determine when the  $90^\circ$  rotation has been completed and feed that information back to the stress generator which will then immediately withdraw the stress [10]. The need for such feedback circuitry makes this strategy unappealing since it introduces additional energy dissipation and complexity.

The clever way to circumvent this problem is to apply a magnetic field in the direction of the minor axis of the nanomagnet, as illustrated in the figure 4.1 of chapter 4 [11], [30], [35], [36]. The magnetic field will dislodge the stable magnetization state from the major axis and place it in two mutually perpendicular orientations in the plane of the magnet. Depending on the sign (say positive) of the magnetostriction coefficient of the material, one sign of stress (tensile) along one of these two axes will make the magnetization rotate to the stable state axis while opposite sign of stress (compressive) will take it to the other stable orientation. Although this scheme has the advantage of switching between two stable states without needing any feedback circuitry, application of magnetic field makes the approach unappealing. Moreover, the angle  $\theta$  between two stable configurations is only  $90^\circ$ . If we employ this scheme to implement a MTJ, the magneto-resistance ratio will be roughly 1.49, considering 70% spin injection/detection efficiency. The resistance ratio is largest when  $\theta = 180^\circ$  and smaller when  $\theta = 90^\circ$ . In fact, if spin injection/detection efficiency is 1, then the resistance ratio is infinite when  $\theta = 180^\circ$  and only 2:1 when  $\theta = 90^\circ$ . Thus, it is imperative to increase  $\theta$  and bring it as close to  $180^\circ$  as possible.

## 5.1 Experimental Setup

Here, we will be showing an experimental demonstration of scheme proposed by our group (see reference [34]) which not only increases  $\theta$  to  $180^\circ$  but also eliminates the bias magnetic field. The experiment was jointly done by me and past group member Dr. Ayan Kumar Biswas. Elliptical Co nanomagnets of  $\sim 180$ - $300$  nm feature size were fabricated on the polished surface of (110)-oriented PMN-PT (10mm by 10mm by 0.5mm) substrate (70% PMN and 30% PT). The PMN-PT substrate was poled initially with an electric field of 0.8 MV/m along the

thickness by applying a positive voltage on the polished surface and a negative voltage on the bottom surface.

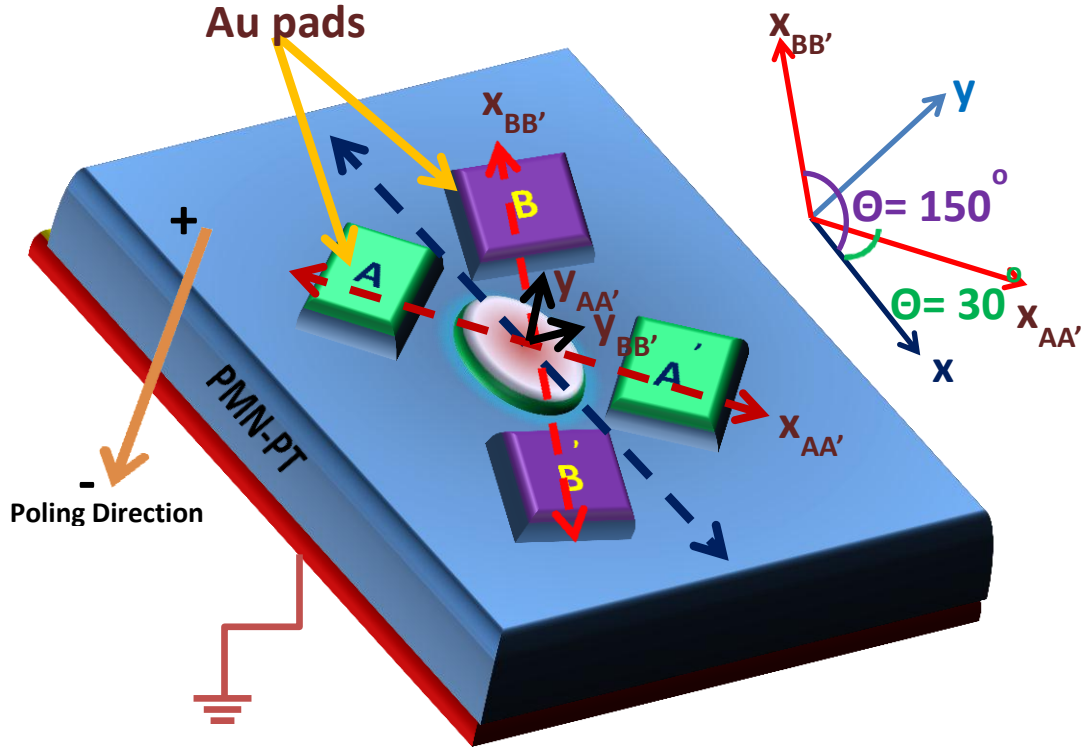


Figure 5.1: Schematic of an elliptical shape nanomagnet and two pairs of square metal pad delineated on PMN-PT substrate (figure is not drawn to scale). The PMN-PT substrate has a dimension of  $(10 \times 10 \times 0.5) \text{ mm}^3$ . The major axis of the nanomagnet is aligned along the x direction. The substrate is poled along the thickness with the polarity shown in figure. Two pairs of Au pad are fabricated with the feature size of  $(400 \times 400 \times 0.08) \text{ }\mu\text{m}^3$ . In each pair, the pads are separated from each other by  $500 \text{ }\mu\text{m}$ , comparable to the thickness of the substrate. the line  $x_{AA'}$ , joining pads in pair AA' subtends an angle of  $30^\circ$  with x axis while line  $x_{BB'}$ , joining the pads in pair BB' subtends an angle of  $150^\circ$ . First, 300 volt is applied between the AA' pair and back electrode (shown in red), then while keeping the AA' activated, 300 volt is applied again between BB' pair and back electrode, next AA' is deactivated, finally BB' is deactivated.

Prior to fabrication of nanomagnets, following the scheme described in ref. [34], two pairs of Au metal pad were patterned and grown by using photolithography and evaporation respectively. Each electrode has the dimension of  $(400 \times 400 \times 0.08) \text{ }\mu\text{m}^3$ . The distance between the electrodes in each pair is around  $0.5 \text{ mm}$ , comparable to the thickness of the substrate. Next, patterns of nanomagnets were delineated by ebeam nanolithography and ferromagnetic Co layer

of nominal thickness 10 nm were deposited by evaporation. The nanomagnets are aligned in such a position that the line joining one pair of electrode is made to subtend an angle  $\sim 30^\circ$  with the common major axis of the nanomagnets while the other pair subtends an angle of  $150^\circ$  as shown in figure 5.1. There is also a  $\sim 4$ nm of Ti adhesion layer underneath each Co layer. This layer is thin enough to transfer most of the strain generated in the PMN-PT layer to the Co layer.

## 5.2 $\sim 180^\circ$ Magnetization Switching

### Case 1: Nanomagnets (198 x 183 x 10) nm<sup>3</sup>

To study the magnetization switching, we first magnetized all Co nanomagnets with a  $\sim 2$  tesla magnetic field along the nominal major axis of the nanomagnets. The magnetization states of the nanomagnets are determined by magnetic force microscopy (MFM) using a low moment tip. Figure 5.2.1 (a) shows AFM images of four such nanomagnets which are 700 nm apart from each other to make dipole interaction among them negligible. The nominal dimensions of these nanomagnets are designed to be (198 x 183 x 10) nm<sup>3</sup>. Figure 5.2.1 (b) shows the MFM images of these nanomagnets before application of stress. It is evident from the figure 5.2.1(b) that after initialization with a magnetic field, the nanomagnets are close to a single domain state but not all of their magnetizations are collinear with the direction of the applied field. This is probably due to the lithographic imperfections or pinning sites which causes the magnetization to rotate to nearby easy axis, closer to the applied field direction. One of the electrode pairs (AA') on the PMN-PT substrate was then subjected to an electric field of 0.6MV/m with the same polarity of the poling field. This generates a highly localized out of plane tensile strain due to  $d_{33}$  coupling and inplane compressive strain due to  $d_{31}$  coupling under the electrode pair. Since the separation between each pair of electrodes are comparable to the substrate thickness (500 micron), the

interaction between the local strain fields will generate a biaxial strain in the PMN-PT substrate underneath the nanomagnets. This method enables us to generate more strain and hence, have better control and higher switching probability of the magnetization of the nanomagnets. Most of the strain is assumed to be transferred from the PMN-PT substrate through the thin adhesion layer of Ti to the Co ferromagnetic layer.

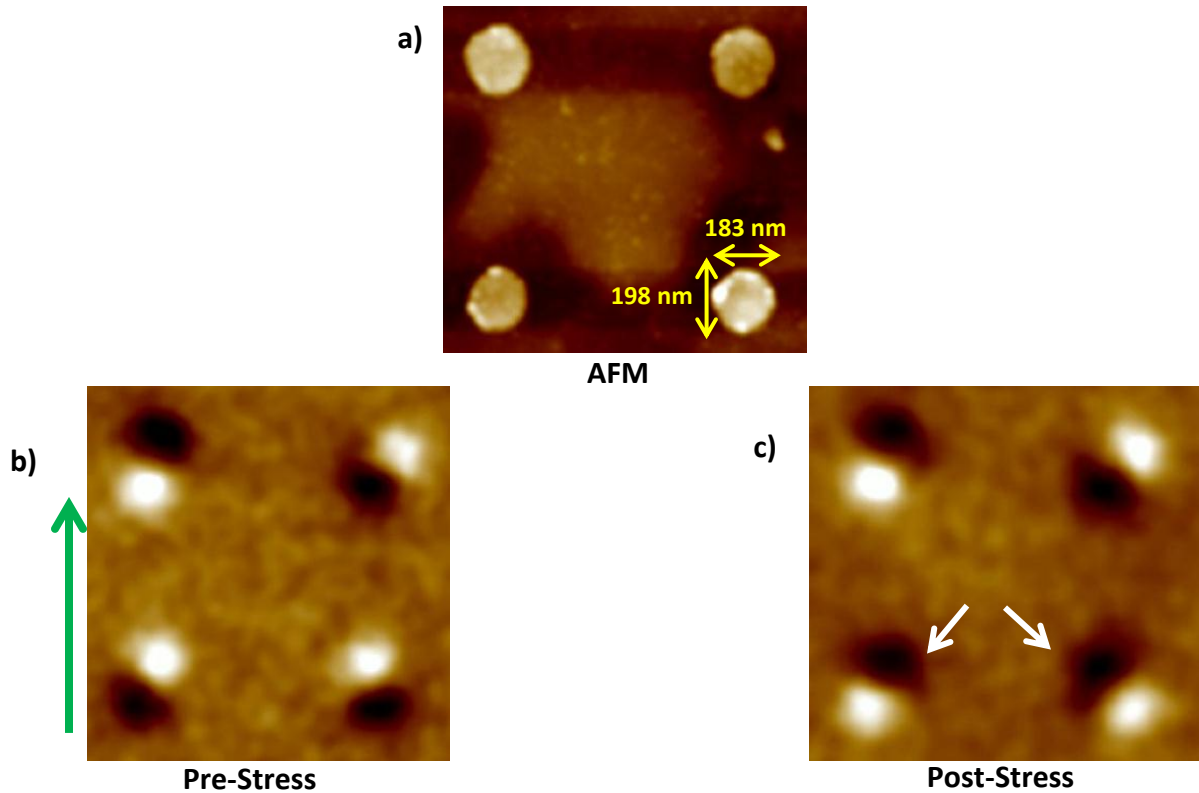


Figure 5.2.1: Atomic force micrographs (AFM) and Magnetic force micrographs (MFM) of nanomagnets of dimensions,  $(198 \times 183 \times 10) \text{ nm}^3$ . a) Top panel shows the topography of the nanomagnets. b) The magnets are initialized with a high magnetic field ( $\sim 2$  Tesla) along the direction of the green arrow as shown in the left panel. After magnetization, the magnetization of the nanomagnets rotated to near by easy axis which subtends a non-zero angle to the original direction of the field. Top left nanomagnet was not properly initialized and got trapped into a stable single domain state aligned in the opposite direction of that of the applied field. Trapping of magnetization can be caused by lithographic imperfections, zagged edges (as evident from AFM image in panel (a)) or defect sites. c) After initialization, a tensile stress was generated in the PMN-PT substrate and transferred to the Co nanomagnets. The panel shows the MFM images of post-stress magnetization states. The magnets in the first row has not shown any rotations while two magnets (marked by white arrow) in the second row has undergone complete  $180^\circ$  rotation from their pre-stress magnetization states.

When the voltage is applied to the AA' pair, the nanomagnets are elongated along the line,  $x_{AA'}$  joining the pair and are contracted along the line,  $y_{AA'}$  (see figure 5.1). Since Co is positive magnetostrictive material, the combination of the biaxial strain ( $\epsilon_{xx}-\epsilon_{yy}$ ) makes  $x_{AA'}$  the hard axis and the magnetization should rotate to the induced easy axis  $y_{AA'}$ . Then, while keeping the AA' electrode pair activated, another electric field of same polarity and 0.6 MV/m was applied to the electrode pair, BB' and simultaneously, the voltage at AA' pair was removed. Similar to the process of AA', upon application of voltage to the pair BB', the magnetization should rotate to the induced easy axis along the  $y_{BB'}$  line from  $x_{BB'}$  (see figure 5.1). After removal of voltage from the BB' pair, the magnetization should rest in the nearest easy axis. This is shown in the figure 5.2.1 (c). The magnetization of two nanomagnets in the top row has remained same. They either rotated but came back to their original orientation after removal of stress, as expected or they did not rotate due to insufficient strain transfer to beat the shape anisotropy barrier, or the magnetization was pinned by defects. However, the other two magnets in the second row have been switched after the application of stress. Clearly in this scenario, the magnetization has been evolved with an electric field from the initial state to final state.

## Case 2: Nanomagnets (294 x 272 x 11) nm<sup>3</sup>

To determine the scalability of this effect, we considered another set of nanomagnets with feature size, (294 x 272 x 11) nm<sup>3</sup> and separation distance, 700 nm. Figure 5.2.2 (a) shows the topography image of 6 similar nanomagnets. MFM images before and after application of stress, have been shown in figure 5.2.2 (b) and (c) respectively. After initialization with a magnetic field, the nanomagnets were oriented in a direction that subtends a non-zero angle with the magnetic field as shown in figure 5.2.2 (b). The post-stress MFM images (see figure 5.2.2 (c))

reveals that the nanomagnets, not indicated by the arrows, show no perceptible difference in their magnetization orientation between pre- and post-stress. On the other hand, the magnets, indicated by the white arrows in figure 5.2.2 (c), have evolved to a new magnetic states. The angular separation of the new magnetic states of the nanomagnets, numbered 1 and 2 in the first row, from their initial state, is  $180^\circ$ . But the nanomagnet, numbered 3 in the second row, has rotated by less than 180 degree, probably due to some pinning sites which ultimately trapped the magnetization states while revolving towards new stable state. The important feature in all of three of them is that their magnetizations have been altered to a new single domain, nonvolatile state by rotating  $\sim 180^\circ$  from the original state with an electric field induced stress, resulting in revolution from one single domain state to another single domain state.

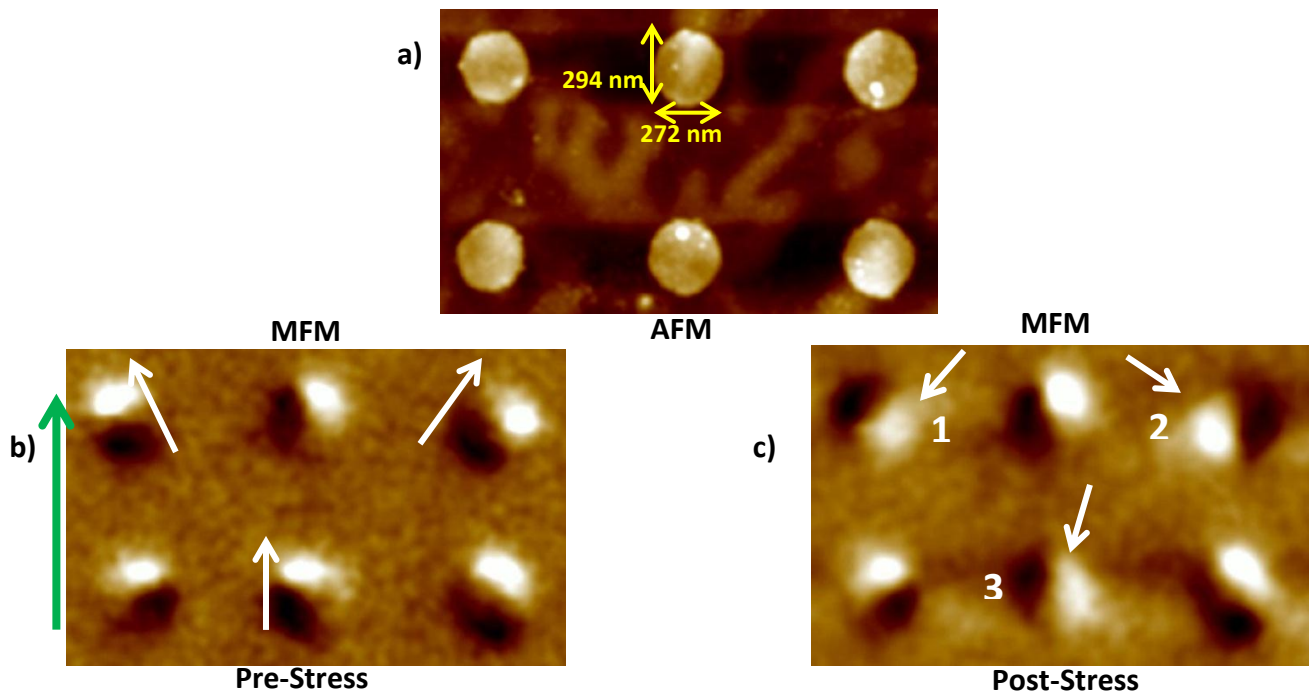


Figure 5.2.2: Atomic force micrographs (AFM) and Magnetic force micrographs (MFM) of nanomagnets of dimensions,  $(294 \times 272 \times 11) \text{ nm}^3$ . Same as figure 3, a) shows the topography of the 4 nanomagnets. b) The magnets are initialized with a  $\sim 2$  Tesla magnetic field along the direction of the green arrow. c) The magnets were subjected to tensile stress. The magnetization of two nanomagnets in the top row (numbered as 1 and 2) have rotated  $180^\circ$  from their respective initial orientations (the initial states subtend a non-zero angle with applied field direction, as marked by white arrows in panel (b)). The nanomagnet, numbered as

3, has rotated less than  $180^\circ$ . It may happen due to pinning sites which might trap the magnetization. However, the newly acquired states of all three nanomagnets are single domain.

### 5.3 Repeatable $180^\circ$ Switching between 2 Stable Orientation

In order to investigate whether the state of magnetization can be switched repeatedly between two stable states, we chose two sets of nanomagnets with feature size, Set A:  $(294 \times 272 \times 11) \text{ nm}^3$  (see figure 5.3 (a,b)), Set B:  $(187 \times 164 \times 9) \text{ nm}^3$  (see figure 5.3 (c,d)). Figure 5.3 (b) illustrates the switching behavior of Set A nanomagnets in three cycles. Cycle 1 shows the initial single domain state of the four nanomagnets. In cycle 2, upon application of tensile stress, top left nanomagnet (marked by white arrow) has evolved to a new state by rotating  $180^\circ$  from the original orientation. The new state is single domain and non-volatile. Next, tensile stress is applied again in cycle 3 and the corresponding MFM images show that the marked nanomagnet has returned to the original state or very close to it. This mechanism corroborates the scheme proposed in ref [34] which predicts successful repeatable switching between two stable states ( $180^\circ$  apart) by applying voltage pulses to two pairs of metal pads successively. The scheme can also be scaled to smaller sizes of nanomagnets, as shown in figure 5.3 (d) where magnets with dimensions (Set B), major axis: 187 nm and minor axis: 164 nm, have undergone similar cycles of stress like Set A magnets. In consecutive panels (see, figure 5.3 (d)), we present initial states of four nanomagnets of similar dimensions, the state after first tension, the state after second tension. The top right nanomagnet (marked by the white arrow in cycle 2), being subjected to tension, has been driven to a new state,  $180^\circ$  apart from its initial state. The second tension cycles brought it back to original state (marked by white arrow in cycle 3).

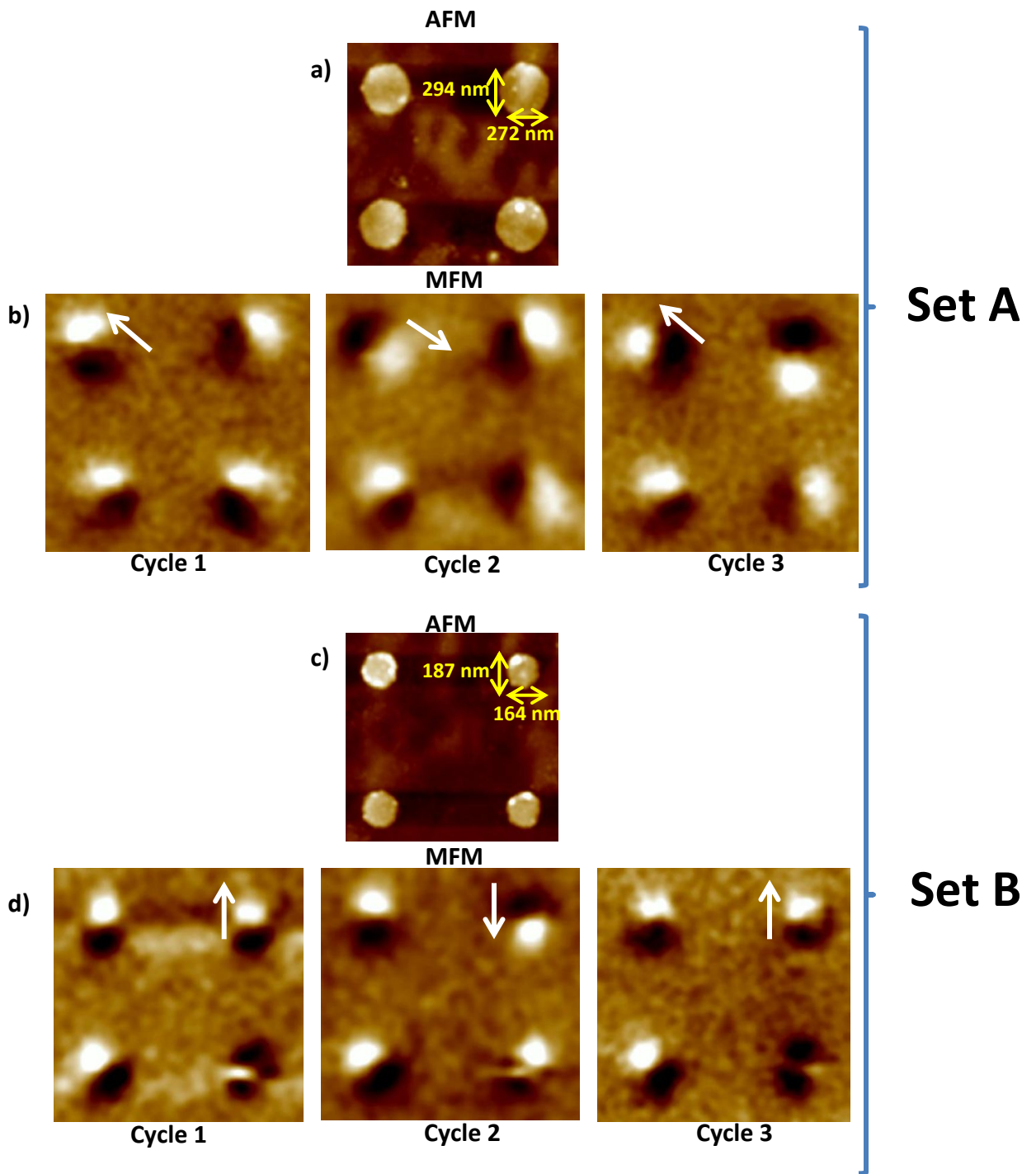


Figure 5.3: Atomic force micrographs (AFM) and Magnetic force micrographs (MFM) of two sets of nanomagnets (Set A and Set B) showing repeatable switching. Set A (a,b): 4 nanomagnets with feature size  $(294 \times 272 \times 11) \text{ nm}^3$ , Set B (c,d): 4 nanomagnets with feature size  $(187 \times 164 \times 9) \text{ nm}^3$ . (a,c) Topography of the 4 isolated nanomagnets with negligible dipole interaction. (b,d) Left most panels show the MFM picture of the initial states; center panels show the MFM image after one tension cycle where nanomagnets (marked by white arrow in (b) and (d)) experienced  $180^\circ$  switching; right most panels show that the nanomagnets marked by white arrows have reverted to their initial orientation after second tension cycle.

Hence, we can define two stable orientations (say, up or down) of the nanomagnets as two logic bits, i.e. up as ‘1’ and down ‘0’; and upon application of tensile stress, we can switch the magnetic orientation from ‘1’ to ‘0’ or ‘0’ to ‘1’, thus realizing ultra-low-energy switching operation in a repeatable manner.

Finally, we calculate the energy dissipation during the switching event in our experiment. We applied 300 V across the 0.5 mm thick PMN-PT substrate corresponds to an electric field of 0.6 MV/m. In our experiment,  $CV^2$  dissipation, the main contributor of energy loss is 255 nJ per sequence where capacitance is  $2 \times 1000 \times 8.854 \times 10^{-12} \times 0.4 \text{ mm} \times 0.4 \text{ mm} / 0.5 \text{ mm} = 2.83 \text{ pF}$  (factor 2 comes from two electrode pads). In straintronic scheme, internal dissipation due to Gilbert damping is almost negligible compared to the  $CV^2$  dissipation. Therefore, the total dissipation a switching event is  $2 \times 255 \text{ nJ} = 510 \text{ nJ}$  for applying stress in two pairs of electrodes. However, if we would have used a PMN-PT substrate of 100 nm thick, and electrode pads of  $100 \text{ nm} \times 100 \text{ nm}$ , the effective capacitance would be  $\sim 2 \times 1000 \times 8.854 \times 10^{-12} \times 100 \text{ nm} \times 100 \text{ nm} / 100 \text{ nm} = 1.7 \text{ fF}$ . The required voltage for switching would reduce to  $0.6 \text{ MV/m} \times 100 \text{ nm} = 60 \text{ mV}$  resulting in a  $CV^2$  loss of  $2 \times 1.7 \text{ fF} \times (60 \text{ mV})^2 = 12.24 \text{ aJ}$  (2955 kT). In contrast to the dissipation in other nanomagnetic switching mechanism such as traditional spin transfer torque (STT) ( $10^7 \text{ kT}$ ) and spin-Hall STT ( $10^4 \text{ kT}$ ), this straintronic version of switching nanomagnets is immensely energy efficient.

## Chapter 6. Conclusion

Numerous proposals to rotate the magnetization of a nanomagnet have been put forward but most of them have failed to deliver the energy efficiency needed to outpace current CMOS technology. Straintronic devices employing magnetostrictive nanomagnet delineated on piezoelectric substrate can offer a solution to this problem by drastically reducing the energy dissipated in the switching event. Switching the magnetization of nanoscale two-phase multiferroics with electrically generated strain has been reported in the past [1], [37], [38]. There is also a report of switching the resistance of a magneto-tunneling junction (MTJ) whose soft layer is a two-phase multiferroic (CoFeB/PMN-PT) with electrically generated strain but the MTJ had tens of nm-scale dimensions (not nanoscale). Most important, all of the above experiments employed ferromagnets with low saturation magnetostriction (Co, Ni, CoFeB), which is not conducive to energy efficiency since the stress needed to rotate the magnetization and correspondingly the voltage needed to generate the stress) is inversely proportional to the magnetostriction coefficient of the magnetostrictive component. In this work, we have investigated how to exploit properties of Galfenol which offers better magnetostriction than most elemental material. We have found the meta-stable behavior in Galfenol which may open the door for multiple bit storage in single nanomagnet.

A core component of straintronic memory is proposed and experimentally demonstrated using Galfenol nanomagnets. There are previous demonstrations of magnetization rotation in FeGa layers with strain [39]–[42], Even more important, none of the above experiments addressed, let alone demonstrate, the “non-toggle” behavior, i.e., the magnetization being driven to one state with one sign of stress/strain and restored back to the other (original) state with the opposite sign of stress/strain. Here, we have achieved this feat.

Finally, we experimentally demonstrated a scheme to realize repeatable  $\sim 180^\circ$  magnetization switching with localized strain which does not require external bias magnetic field and promises to deliver a high magneto-resistance ratio. This method can be scaled down to nano-dimensions enabling access to individual magnetic tunneling junction comprising nanomagnet grown on piezoelectric layer and portends an ultra-energy-efficient non-volatile memory.

In fine, this research opens the door for new possibilities to further advance the field of spintronics in realizing ultra-energy-efficient logic and memory devices to sustain the Moore's Law beyond 2020.

## List of references:

- [1] N. D'Souza, M. Salehi Fashami, S. Bandyopadhyay, and J. Atulasimha, "Experimental Clocking of Nanomagnets with Strain for Ultralow Power Boolean Logic," *Nano Lett.*, vol. 16, no. 2, pp. 1069–1075, Feb. 2016.
- [2] S. A. Wolf, D. D. Awschalom, R. A. Buhrman, J. M. Daughton, S. von Molnár, M. L. Roukes, A. Y. Chtchelkanova, and D. M. Treger, "Spintronics: A Spin-Based Electronics Vision for the Future," *Science*, vol. 294, no. 5546, pp. 1488–1495, Nov. 2001.
- [3] M. S. Fashami, J. Atulasimha, and S. Bandyopadhyay, "Magnetization dynamics, throughput and energy dissipation in a universal multiferroic nanomagnetic logic gate with fan-in and fan-out," *Nanotechnology*, vol. 23, no. 10, p. 105201, 2012.
- [4] M. T. Alam, M. J. Siddiq, G. H. Bernstein, M. Niemier, W. Porod, and X. S. Hu, "On-Chip Clocking for Nanomagnet Logic Devices," *IEEE Trans. Nanotechnol.*, vol. 9, no. 3, pp. 348–351, May 2010.
- [5] D. C. Ralph and M. D. Stiles, "Spin transfer torques," *J. Magn. Magn. Mater.*, vol. 320, no. 7, pp. 1190–1216, Apr. 2008.
- [6] M. Yamanouchi, D. Chiba, F. Matsukura, and H. Ohno, "Current-induced domain-wall switching in a ferromagnetic semiconductor structure," *Nature*, vol. 428, no. 6982, pp. 539–542, Apr. 2004.
- [7] S. Fukami, T. Suzuki, K. Nagahara, N. Ohshima, Y. Ozaki, S. Saito, R. Nebashi, N. Sakimura, H. Honjo, K. Mori, C. Igarashi, S. Miura, N. Ishiwata, and T. Sugibayashi, "Low-current perpendicular domain wall motion cell for scalable high-speed MRAM," in *2009 Symposium on VLSI Technology*, 2009, pp. 230–231.
- [8] P. K. Amiri and K. L. Wang, "Voltage-controlled magnetic anisotropy in spintronic devices," *SPIN*, vol. 2, no. 3, p. 1240002, Sep. 2012.
- [9] L. Liu, C.-F. Pai, Y. Li, H. W. Tseng, D. C. Ralph, and R. A. Buhrman, "Spin-Torque Switching with the Giant Spin Hall Effect of Tantalum," *Science*, vol. 336, no. 6081, pp. 555–558, May 2012.
- [10] K. Roy, S. Bandyopadhyay, and J. Atulasimha, "Hybrid spintronics and straintronics: A magnetic technology for ultra low energy computing and signal processing," *Appl. Phys. Lett.*, vol. 99, no. 6, p. 63108, 2011.
- [11] S. Bandyopadhyay and M. Cahay, *Introduction to Spintronics*, 1 edition. Boca Raton: CRC Press, 2008.
- [12] G. Salis, R. Wang, X. Jiang, R. M. Shelby, S. S. P. Parkin, S. R. Bank, and J. S. Harris, "Temperature independence of the spin-injection efficiency of a MgO-based tunnel spin injector," *Appl. Phys. Lett.*, vol. 87, no. 26, p. 262503, Dec. 2005.
- [13] K. Roy, S. Bandyopadhyay, and J. Atulasimha, "Binary switching in a 'symmetric' potential landscape," *Sci. Rep.*, vol. 3, p. 3038, Oct. 2013.
- [14] J. Cui, J. L. Hockel, P. K. Nordeen, D. M. Pisani, C. Liang, G. P. Carman, and C. S. Lynch, "A method to control magnetism in individual strain-mediated magnetoelectric islands," *Appl. Phys. Lett.*, vol. 103, no. 23, p. 232905, Dec. 2013.
- [15] "Hybrid spintronics and straintronics: A magnetic technology for ultra low energy computing and signal processing." [Online]. Available: <http://scitation.aip.org/content/aip/journal/apl/99/6/10.1063/1.3624900>. [Accessed: 03-Jun-2016].

- [16] M. Barangi and P. Mazumder, "Straintronics: A leap toward ultimate energy efficiency of magnetic random access memories.," *IEEE Nanotechnol. Mag.*, vol. 9, no. 3, pp. 15–24, Sep. 2015.
- [17] K. Roy, S. Bandyopadhyay, and J. Atulasimha, "Energy dissipation and switching delay in stress-induced switching of multiferroic nanomagnets in the presence of thermal fluctuations," *J. Appl. Phys.*, vol. 112, no. 2, p. 23914, Jul. 2012.
- [18] Q. Xing, Y. Du, R. J. McQueeney, and T. A. Lograsso, "Structural investigations of Fe–Ga alloys: Phase relations and magnetostrictive behavior," *Acta Mater.*, vol. 56, no. 16, pp. 4536–4546, Sep. 2008.
- [19] A. E. Clark, K. B. Hathaway, M. Wun-Fogle, J. B. Restorff, T. A. Lograsso, V. M. Keppens, G. Petculescu, and R. A. Taylor, "Extraordinary magnetoelasticity and lattice softening in bcc Fe-Ga alloys," *J. Appl. Phys.*, vol. 93, no. 10, p. 8621, 2003.
- [20] "Journal of Applied Physics - Volume 105, Issue 7." [Online]. Available: <http://scitation.aip.org/content/aip/journal/jap/105/7>. [Accessed: 03-Jun-2016].
- [21] B. Adolphi, J. McCord, M. Bertram, C.-G. Oertel, U. Merkel, U. Marschner, R. Schäfer, C. Wenzel, and W.-J. Fischer, "Improvement of sputtered Galfenol thin films for sensor applications," *Smart Mater. Struct.*, vol. 19, no. 5, p. 55013, Mar. 2010.
- [22] M. E. Jamer, B. A. Assaf, S. P. Bennett, L. H. Lewis, and D. Heiman, "Magnetic properties and large coercivity of  $Mn_xGa$  nanostructures," *J. Magn. Magn. Mater.*, vol. 358–359, pp. 259–262, May 2014.
- [23] H. D. Chopra and M. Wuttig, "Non-Joulian magnetostriction," *Nature*, vol. 521, no. 7552, pp. 340–343, May 2015.
- [24] J. Kelly, M. Leonard, C. Tantigate, and A. Safari, "Effect of Composition on the Electromechanical Properties of  $(1-x)Pb(Mg_{1/3}Nb_{2/3})O_3-xPbTiO_3$  Ceramics," *J. Am. Ceram. Soc.*, vol. 80, no. 4, pp. 957–964, Apr. 1997.
- [25] Z. Xia, L. Wang, W. Yan, Q. Li, and Y. Zhang, "Comparative investigation of structure and dielectric properties of  $Pb(Mg_{1/3}Nb_{2/3})O_3-PbTiO_3$  (65/35) and 10%  $PbZrO_3$ -doped  $Pb(Mg_{1/3}Nb_{2/3})O_3-PbTiO_3$  (65/35) ceramics prepared by a modified precursor method," *Mater. Res. Bull.*, vol. 42, no. 9, pp. 1715–1722, Sep. 2007.
- [26] N. A. Morley, A. Javed, and M. R. J. Gibbs, "Effect of a forming field on the magnetic and structural properties of thin Fe–Ga films," *J. Appl. Phys.*, vol. 105, no. 7, p. 07A912, Apr. 2009.
- [27] H. Ahmad, J. Atulasimha, and S. Bandyopadhyay, "Electric field control of magnetic states in isolated and dipole-coupled FeGa nanomagnets delineated on a PMN-PT substrate," *Nanotechnology*, vol. 26, no. 40, p. 401001, Sep. 2015.
- [28] A. K. Biswas, S. Bandyopadhyay, and J. Atulasimha, "Energy-efficient magnetoelastic non-volatile memory," *Appl. Phys. Lett.*, vol. 104, no. 23, p. 232403, Jun. 2014.
- [29] A. K. Biswas, J. Atulasimha, and S. Bandyopadhyay, "An error-resilient non-volatile magneto-elastic universal logic gate with ultralow energy-delay product," *Sci. Rep.*, vol. 4, p. 7553, Dec. 2014.
- [30] N. Tiercelin, Y. Dusch, V. Preobrazhensky, and P. Pernod, "Magnetolectric memory using orthogonal magnetization states and magnetoelastic switching," *J. Appl. Phys.*, vol. 109, no. 7, p. 07D726, Apr. 2011.
- [31] H. Ahmad, J. Atulasimha, and S. Bandyopadhyay, "Reversible strain-induced magnetization switching in FeGa nanomagnets: Pathway to a rewritable, non-volatile, non-toggle, extremely low energy straintronic memory," *Sci. Rep.*, vol. 5, p. 18264, Dec. 2015.

- [32] S. Datta, J. Atulasimha, C. Mudivarthi, and A. B. Flatau, "Stress and magnetic field-dependent Young's modulus in single crystal iron-gallium alloys," *J. Magn. Magn. Mater.*, vol. 322, no. 15, pp. 2135–2144, Aug. 2010.
- [33] J. Cui, C.-Y. Liang, E. A. Paisley, A. Sepulveda, J. F. Ihlefeld, G. P. Carman, and C. S. Lynch, "Generation of localized strain in a thin film piezoelectric to control individual magnetoelectric heterostructures," *Appl. Phys. Lett.*, vol. 107, no. 9, p. 92903, Aug. 2015.
- [34] A. K. Biswas, S. Bandyopadhyay, and J. Atulasimha, "Complete magnetization reversal in a magnetostrictive nanomagnet with voltage-generated stress: A reliable energy-efficient non-volatile magneto-elastic memory," *Appl. Phys. Lett.*, vol. 105, no. 7, p. 72408, Aug. 2014.
- [35] S. Giordano, Y. Dusch, N. Tiercelin, P. Pernod, and V. Preobrazhensky, "Combined nanomechanical and nanomagnetic analysis of magnetoelectric memories," *Phys. Rev. B*, vol. 85, no. 15, p. 155321, Apr. 2012.
- [36] S. Giordano, Y. Dusch, N. Tiercelin, P. Pernod, and V. Preobrazhensky, "Thermal effects in magnetoelectric memories with stress-mediated switching," *J. Phys. Appl. Phys.*, vol. 46, no. 32, p. 325002, 2013.
- [37] T.-K. Chung, S. Keller, and G. P. Carman, "Electric-field-induced reversible magnetic single-domain evolution in a magnetoelectric thin film," *Appl. Phys. Lett.*, vol. 94, no. 13, p. 132501, Mar. 2009.
- [38] M. Buzzi, R. V. Chopdekar, J. L. Hockel, A. Bur, T. Wu, N. Pilet, P. Warnicke, G. P. Carman, L. J. Heyderman, and F. Nolting, "Single Domain Spin Manipulation by Electric Fields in Strain Coupled Artificial Multiferroic Nanostructures," *Phys. Rev. Lett.*, vol. 111, no. 2, p. 27204, Jul. 2013.
- [39] J. L. Weston, A. Butera, T. Lograsso, M. Shamsuzzoha, I. Zana, G. Zangari, and J. Barnard, "Fabrication and characterization of Fe<sub>81</sub>Ga<sub>19</sub> thin films," *IEEE Trans. Magn.*, vol. 38, no. 5, pp. 2832–2834, Sep. 2002.
- [40] R. R. Basantkumar, B. J. H. Stadler, W. P. Robbins, E. M. Summers, R. R. Basantkumar, B. J. H. Stadler, W. P. Robbins, and E. M. Summers, "Integration of Thin-Film Galfenol With MEMS Cantilevers for Magnetic Actuation," *IEEE Trans. Magn.*, vol. 42, no. 10, pp. 3102–3104, Oct. 2006.
- [41] P. Zhao, Z. Zhao, D. Hunter, R. Suchoski, C. Gao, S. Mathews, M. Wuttig, and I. Takeuchi, "Fabrication and characterization of all-thin-film magnetoelectric sensors," *Appl. Phys. Lett.*, vol. 94, no. 24, p. 243507, Jun. 2009.
- [42] T. Brintlinger, S.-H. Lim, K. H. Baloch, P. Alexander, Y. Qi, J. Barry, J. Melngailis, L. Salamanca-Riba, I. Takeuchi, and J. Cumings, "In Situ Observation of Reversible Nanomagnetic Switching Induced by Electric Fields," *Nano Lett.*, vol. 10, no. 4, pp. 1219–1223, Apr. 2010.